Contents lists available at ScienceDirect

Remote Sensing of Environment

Global burned area mapping from Sentinel-3 Synergy and VIIRS active fires

Joshua Lizundia-Loiola [a,b,*], Magí Franquesa [a], Amin Khairoun [a], Emilio Chuvieco [a]

[a] *Universidad de Alcalá, Environmental Remote Sensing Research Group, Department of Geology, Geography and the Environment, Calle Colegios 2, Alcalá de Henares 28801, Spain*
[b] *TECNALIA, Basque Research and Technology Alliance (BRTA), Parque Tecnológico de Bizkaia, Astondo Bidea, Edificio 700, Derio 48160, Spain*

ARTICLE INFO

ABSTRACT

After more than two decades of successful provision of global burned area data the MODIS mission is near to its end. Therefore, using alternative images to generate moderate resolution burned area maps becomes critical to guarantee temporal continuity of these products. This paper presents the development of a hybrid algorithm based on Copernicus Sentinel-3 (S3) Synergy (SYN) data and Visible Infrared Imaging Radiometer Suite (VIIRS) 375 m active fires for global detection of burned areas. Using the synergistic and co-located measurements of OLCI and SLSTR instruments on board S3A and S3B, the SYN product offers global, near-daily surface reflectance data at 300 m for both sensors. Our algorithm relied on SYN shortwave infrared (SWIR) bands to compute a multi-temporal separability index that enhanced the burn signal. Active fires from the VIIRS sensor were used to generate spatio-temporal clusters for determining local detection thresholds. Active fires were filtered from those thresholds to obtain the seeds from which a contextual growing was applied to extract burned patches. The algorithm was processed globally for 2019 data to generate a new burned area product, named FireCCIS310. Based on a stratified random sampling, error estimates showed an important reduction of omission errors versus other global burned area products while keeping the commission errors at a similar level (Oe = 41.2% $\pm$ 3.0%, Ce = 19.2% $\pm$ 1.7%). The new FireCCIS310 dataset included 4.99 million km^2 for the year 2019, which implied around 1 million more than the precursor FireCCI51 product, based on MODIS 250 m reflectance values. Temporal reporting accuracy was improved as well, detecting 53% of the burned pixels within a 0–1 day difference. Besides, the new product was much less affected by the border effects than FireCCI51, as a result of an improved active fire filtering process. The FireCCIS310 product is accessible through the CCI Open Data Portal (https://climate.esa.int/es/odp/#/dashboard, last accessed on July 2022).

1. Introduction

Monitoring of burned areas is crucial to better understand the role of fire in the Earth's System. The analysis of the spatio-temporal patterns of biomass burning can help us to assess the relationship between fire and vegetation recovery (Bright et al., 2019), biodiversity (Kelly and Brotons, 2017), land management and deforestation (Andela et al., 2017; Fanin and van der Werf, 2015), and human health (Reid et al., 2016). In addition, fire disturbance is considered an Essential Climate Variable (ECV), because of its impacts on atmospheric emissions and carbon stocks (Abatzoglou et al., 2018; van der Werf et al., 2017).

The range of satellite systems used for burned area mapping is quite diverse, including global and local scales, with different spectral, temporal, and spatial resolutions (Chuvieco et al., 2019). Temporal

resolution directly affects not only how accurately the actual time of burn is assigned, but also the capacity for observing the burned areas since, as time after the fire passes, the burned signal weakens due to vegetation recovery and ash removal (Melchiorre and Boschetti, 2018). At least daily temporal coverage is critical for an accurate detection of the burning date and for near-real-time monitoring of burned areas (Urbanski et al., 2018). This also affects the delimitation of individual burned patches and derived parameters such as fire rate of spread or direction and detection of ignition points (Andela et al., 2019; Laurent et al., 2018). The spatial resolution defines the size of the smallest object that can be resolved by the sensor, which limits the detection of small fires (< 100 ha) (Ramo et al., 2021). While medium spatial resolutions of 10–30 m have shown promising results in terms of spatial accuracy (Hawbaker et al., 2020; Long et al., 2019; Roteta et al., 2019; Roy et al.,

2019) and the growing availability of free images from the Landsat and the Sentinel-2 missions has made them more attractive, there remains the obstacle of the huge processing effort needed to obtain global long-term products. Therefore, global burned area products still rely on moderate resolution sensors, with 250–500 m pixel sizes and 1–2 days revisit time.

One of the most relevant sensors for global burned area mapping has been the Moderate Resolution Imaging Spectroradiometer (MODIS) aboard Terra and Aqua satellites, which has been the basis for both burned area and active fire products. The standard NASA global burned area product MCD64A1 c6 is obtained from a hybrid algorithm that combines a vegetation index based on daily shortwave infrared (SWIR) reflectance data at 500 m and MODIS 1-km active fire data (Giglio et al., 2018; Giglio et al., 2009). Within the ESA Climate Change Initiative's FireCCI project another global burned area product (called FireCCI51) based on MODIS active fires and 250 m near-infrared (NIR) band was released (Chuvieco et al., 2018; Lizundia-Loiola et al., 2020).

After more than two decades of mission, Terra satellite's exit from the Earth Science Constellation is predicted for October 2022 (https://terra.nasa.gov/news/terra-begins-to-drift-in-time, last accessed on July 2022), affecting the platform's altitude and, hence, its mean local time of crossing, spatial coverage, and spatial resolution. This will greatly impact the above-mentioned global burned area products and, thus, the scientific community that relies on their quality. The adaptation of these MODIS-based algorithms and products to new satellites and sensors to ensure provision of burned area products into the future is, therefore, a relevant and challenging topic.

The Suomi National Polar-orbiting Partnership (S-NPP) (launched in 2011) and the NOAA-20 (launched in 2017) satellites aimed to provide continuity for key data series observations initiated by NASA's Terra and Aqua missions. More specifically, the Visible Infrared Imaging Radiometer Suite (VIIRS) aboard these satellites was developed from the experience of previous sensors, particularly from MODIS. Depending on the latitude its large image swath (3000 km) and relatively short revisit time (12h) ensure at least two observations a day in 22 spectral bands at 375 m and 750 m (Justice et al., 2013). Two active fire detection products, at 375 and 750 m, are currently produced based on VIIRS data (Csiszar et al., 2014; Schroeder et al., 2014). Several studies have explored the use of this information for detecting burned area (Fernández-Manso and Quintano, 2020; Oliva and Schroeder, 2015; Santos et al., 2020; Urbanski et al., 2018), showing that VIIRS active fires may be a suitable replacement for the MODIS active fires in hybrid burned area algorithms.

From the European side, the Copernicus Sentinel-3 A (S3A) and B (S3B) satellites can also provide sound alternatives for the continuity of global fire products. The FireCCI51 algorithm, for instance, was recently adapted to the Ocean and Land Colour Instrument (OLCI) data by replacing MODIS NIR with the most similar OLCI NIR band at 300 m (Lizundia-Loiola et al., 2021). The new Copernicus Climate Change Service burned area product (named C3SBA11) showed consistent results in terms of global correlation with FireCCI51, confirming the capacity of OLCI to detect similar burned area to MODIS, although still relying on MODIS active fires. However, the C3SBA11 product offered low temporal reporting accuracy (only 17.4% of burned pixels were detected within 1 day) and showed some border effects that were derived from the tile-oriented processing used to run the algorithm globally (Lizundia-Loiola et al., 2021). In addition to OLCI, the S3 satellites carry the Sea and Land Surface Temperature Radiometer (SLSTR) sensor, which includes SWIR bands, providing a better detection of post-fire changes. Although the original resolution of this sensor is 500 m, ESA has developed a synthetic product, named Sentinel-3 Synergy (SYN), which combines OLCI and SLSTR spectral bands at 300 m resolution (Henocq et al., 2018). SLSTR can also be used to detect active fires at 1 km resolution based on its middle and thermal infrared bands. A full daytime version was released in 2021, although for now only the night-time version is available as standard global, monthly summarised files

(https://cds.climate.copernicus.eu/cdsapp#!/dataset/satellite-fire-radiative-power?tab=overview, last accessed July 2022). The SLSTR sensor can complement MODIS or VIIRS active fire information (Xu et al., 2021).

This paper presents the development of a global burned area algorithm based on SYN reflectance and VIIRS 375 m active fire products. This hybrid algorithm demonstrates the capability of the SYN surface reflectance product to detect burned area globally and overcomes some of the limitations found in the precursor FireCCI51 product, particularly the low temporal reporting accuracy and border effects between tiles. The new algorithm, named FireCCIS310, was spatially validated based on Landsat imagery that was selected following a stratified random sampling, while the temporal dimension was validated by comparing the day of detection with MODIS and VIIRS active fires. The spatial distribution of global burned area was compared to the FireCCI51, C3SBA11, and MCD64A1 c6 products.

2. Methods

2.1. Algorithm overview

The FireCCIS310 algorithm is displayed schematically in Fig. 1 and explained in subsequent sections. It follows a hybrid approach, which has shown to be one of the most reliable methodologies to detect burned area globally (Alonso-Canas and Chuvieco, 2015; Campagnolo et al., 2019; Chuvieco et al., 2018; Giglio et al., 2018; Giglio et al., 2009; Lizundia-Loiola et al., 2021; Lizundia-Loiola et al., 2020). Thermal anomalies provide an accurate location and timing of the active fires due to their high thermal contrast with the surrounding areas (Giglio et al., 2016; Schroeder et al., 2014). Conversely, changes in surface reflectance are more persistent both in space and time, providing the chance to detect the entire burned patch. Hybrid algorithms combine the strengths of both thermal anomalies and changes in surface reflectance data to reliably detect burned area.

Daily time-series of the vegetation index Normalized Burn Ratio 2 or NBR2 (derived from Trigg and Flasse (2001)) were used to derive a separability index that enhances the burn signal. This separability index was maximised to select within a given month the day with the highest probability of being burned. Based on the selected days, four monthly variables were derived: maximum separability, NBR2 change, texture, and day difference. The texture determined the temporal coherence of adjacent pixels, while the day difference accounted for the consistency between the day of maximum separability and the nearest active fire date. Additionally, active fire clusters were defined considering their spatio-temporal proximity (Lizundia-Loiola et al., 2020). Then, a two-phase methodology was applied to detect burned area (Bastarrika et al., 2011). First, seed pixels were selected based on active fires and cluster-adapted thresholds. This step aimed to reduce commission errors by selecting only those pixels that showed a clear burned signal. In a second step, a contextual growing was applied from the seeds, using the cluster-adapted thresholds to stop it. This last step aimed to reduce omission errors by detecting the entire burned patch.

Some of the steps of the algorithm used a global parametrisation to guide the detection process. The definition of those global parameters was based on the reference perimeters that were generated for the calibration areas (Section 2.2) and the knowledge coming from other global burned area products.

The processing units were defined as tiles of 10° x 10° (3600 × 3600 pixels) and a total of 273 tiles were processed (Fig. 2). The algorithm was run for the year 2019 based on SYN images from both S3A and B. The outputs of the FireCCIS310 algorithm were formatted following the standards of the FireCCI project (Chuvieco et al., 2018) and are accessible through the CCI Open Data Portal (https://climate.esa.int/es/odp/#/dashboard, last accessed on July 2022).
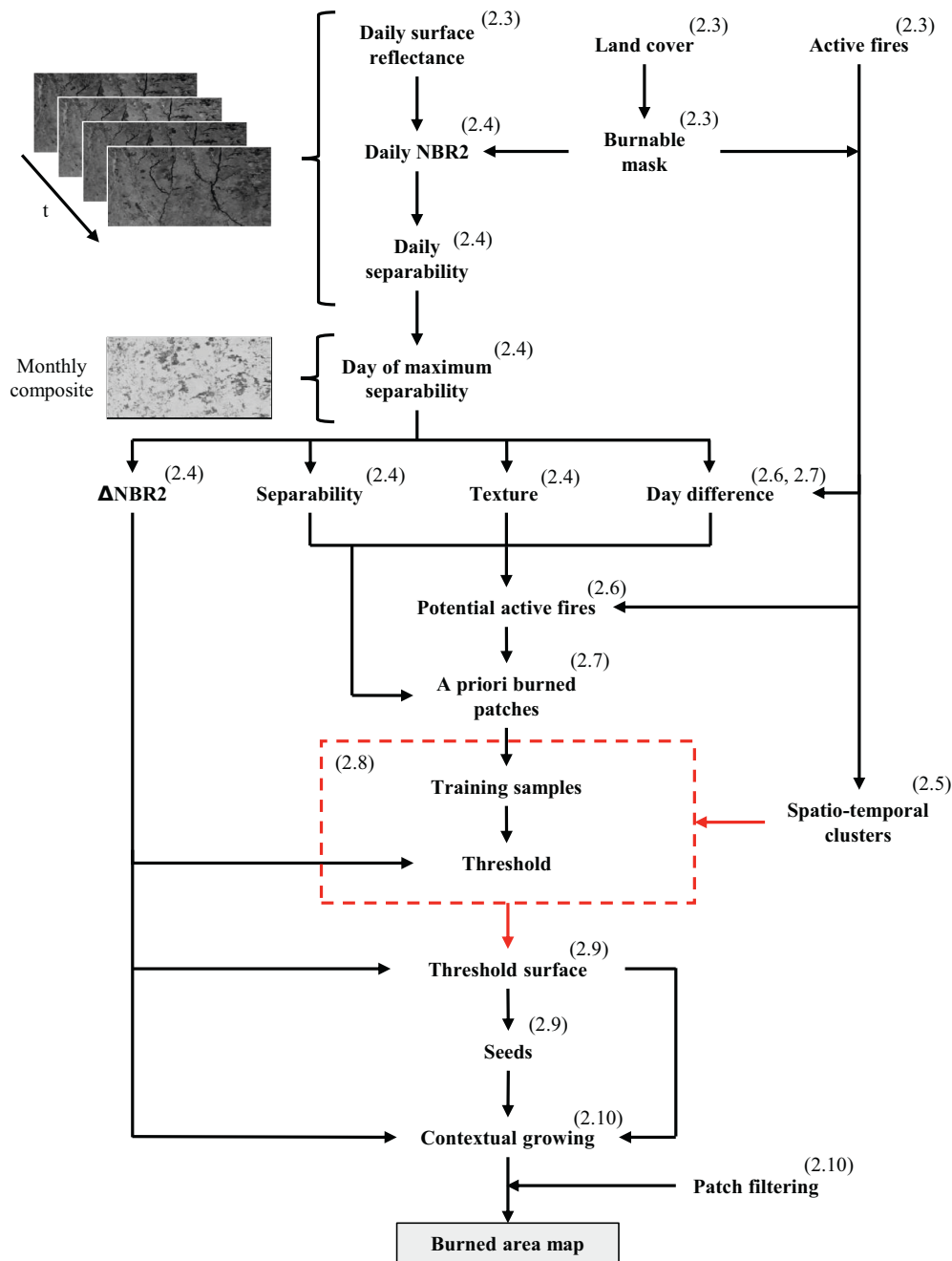
Fig. 1. Main structure of the FireCCIS310 algorithm. In parenthesis the section where the step was explained. The red dotted box means that those steps were repeated for each active fires spatio-temporal cluster. (For interpretation of the references to colour in this figure legend, the reader is referred to the web version of this article.)

2.2. Calibration sites

Global burned area mapping algorithms must be able to deal with the great diversity of fire regimes found around the world. To represent that diversity, 13 S3 tiles were selected for algorithm calibration. The selected sites were distributed across the main biomes. Two tiles were located in Canada and included boreal forests. Another two were placed on the western coast of the United States, in the Mediterranean area of California. Five tiles were located in tropical savannas, the biome with the highest fire activity, but in different continents: one in the Colombian Llanos, two in Africa (one per hemisphere), and two in northern Australia. In Africa another tile was included that encompassed a transition zone between tropical savanna and tropical forest. Additionally, a

tile in Kazakhstan was used as representative of deserts and xeric shrublands biome. The last two tiles were placed in Far East Russia and mainly included temperate forests and savannas.

Reference perimeters were generated for 43 Landsat scenes distributed within 12 of the 13 tiles (Fig. 2). Landsat 8 images acquired during 2019 were used to extract reference perimeters following the methodology described in Roteta et al. (2021) and Franquesa et al. (2022). Only Landsat pairs where fire activity was observed were interpreted. In the case of the tile located in Colombia, no cloud-free images were available, but it was still used to visually check if any unexpected behaviour arose. For clarification, it should be noted that these reference perimeters were produced ad hoc for the calibration areas and were independent from those used for validation purposes
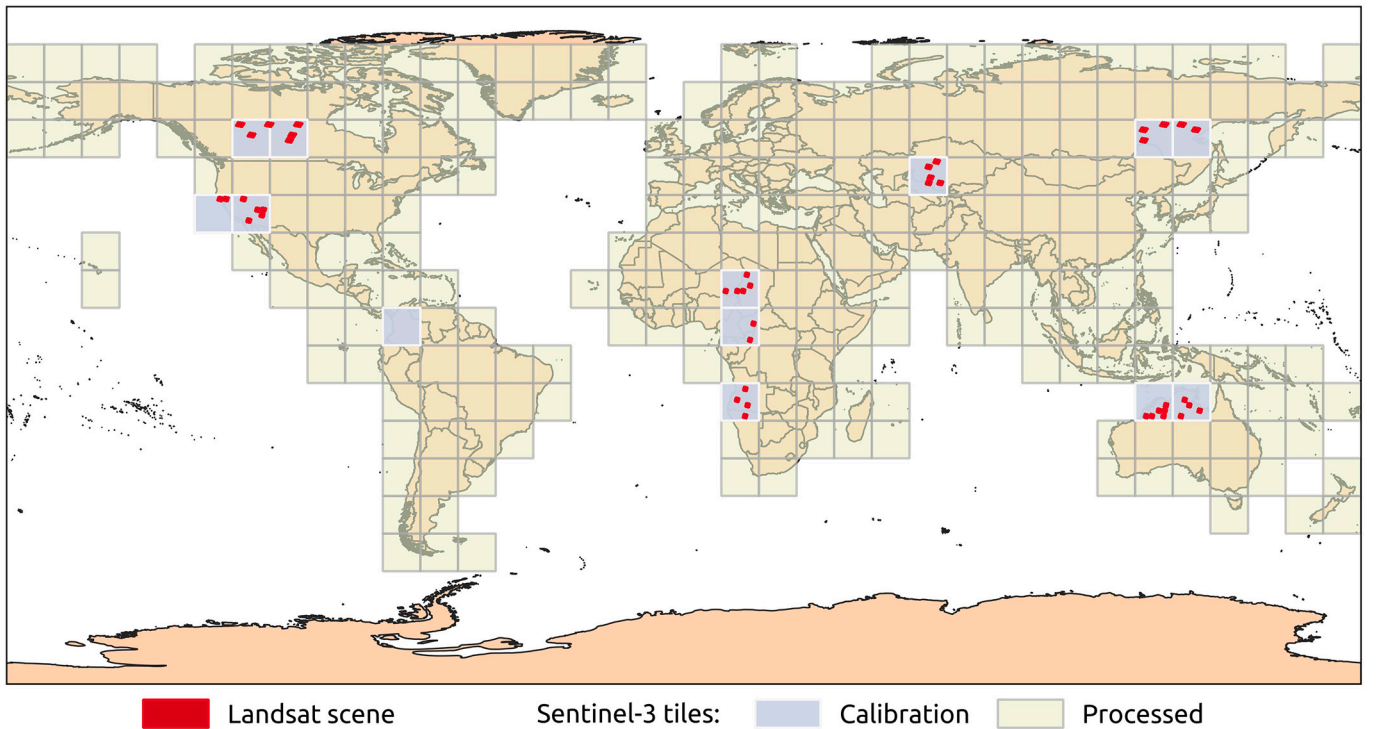
Fig. 2. Tiling system and calibration areas used to develop the FireCCIS310 algorithm.

2.3. Input data

The main input data sources of the algorithm presented in this paper were S3 SYN surface reflectance and S-NPP VIIRS active fires. Based on the synergistic and co-located measurements of the OLCI and SLSTR optical instruments, the SYN Level 2 product (SY_2_SYN) provides surface reflectance and aerosol parameters over land at 300 m for all OLCI and SLSTR bands, excluding OLCI O2 and Water Vapour absorption bands and SLSTR cloud detection (1374 nm) and thermal bands. This product provides continuity to the surface vegetation products obtained from the VEGETATION instrument aboard the Satellite Pour l'Observation de la Terre (SPOT) and the PROBA-V mission. The SYN product is generated for both S3 satellites in operation: S3A (launched on 2016) and B (launched on 2018). These satellites have a near-polar sun-synchronous orbit with an equatorial crossing at 10:00 h (Mean Local Solar Time). The SYN swath is limited to the common area between OLCI and SLSTR swaths (~1270 km), providing a near-daily global coverage from November 2018 onwards. A pre-processing was applied to generate daily composites at 300 m that follow the tiling system shown in Fig. 2. When a particular pixel was observed several times during the same day, the most nadiral observation was retained. Among the bands provided by the resulting SYN daily product, two were used to detect burned area: SLSTR band 5 (labelled as SDR_S5N), which provides information in the short SWIR (SSWIR) centred at 1613.40 nm, and SLSTR band 6 (labelled as SDR_S6N), which belongs to the long SWIR (LSWIR) centred at 2255.70 nm.

VIIRS active fires at 375 m resolution were extracted from the VNP14IMGML product (Schroeder and Giglio, 2018), whose time series begins in January 2012. This product provides global monthly fire location data in ASCII format, along with essential fire detection information. The "Type" field, which identifies the type of thermal anomaly, was used to select only those locations labelled as "presumed vegetation fire" (value equal to zero).

The only auxiliary data used by the algorithm was the Land Cover (LC) v2.1.1 distributed by the Copernicus Climate Change Service (https ://cds.climate.copernicus.eu/cdsapp#!/dataset/satellite-land-cover? tab=overview, last accessed July 2022), which is a continuation of the product developed in the Land Cover CCI project (Defourny et al., 2017). This dataset provides global, annual land cover maps since 1992 at 300 m spatial resolution, distinguishing among 22 land cover classes that were defined using the United Nations Food and Agriculture Organization's (UN FAO) Land Cover Classification System (LCCS). The LC data was used to exclude from further processing the unburnable areas, i.e. regions identified as urban and bare areas, water bodies and permanent snow and ice, and to identify the LC class of the burned pixels in the post-processing. To represent the situation prior to the fire the previous year's land cover map was used.

2.4. Temporal compositing

Temporal composites are used in burned area mapping algorithms to overcome problems derived from clouds, angular effects or reception issues found in daily images. The composition selects the cleanest observation, while enhancing the burned signal (Barbosa et al., 1998; Chuvieco et al., 2005; Sousa et al., 2003). They tend to increase the separability between burned and unburned classes to facilitate burned pixel classification (Alonso-Canas and Chuvieco, 2015; Giglio et al., 2009). The FireCCIS310 algorithm generated monthly composites based on a separability index (S) that was derived from daily time series of NBR2:

$$S(t,x,y) = \frac{-\Delta NBR2(t,x,y)}{\left| \sigma_{pre}(t,x,y) + \sigma_{post}(t,x,y) \right| / 2} \tag{1}$$

$$\Delta NBR2(t,x,y) = NBR2_{post}(t,x,y) - NBR2_{pre}(t,x,y)$$

The NBR2 is a vegetation index expressed as the normalized ratio between the SSWIR and LSWIR:

$$NBR2 = \frac{\rho_{SSWIR} - \rho_{LSWIR}}{\rho_{SSWIR} + \rho_{LSWIR}} \tag{2}$$

where the corresponding SYN bands were ρ_{SSWIR} = SDR_S5N (1613.40 nm) and ρ_{LSWIR} = SDR_S6N (2255.70 nm).

The separability index *S* was first proposed by Giglio et al. (2009) for a vegetation index derived from MODIS NIR-SWIR bands centred at 1240 nm and 2130 nm. In the case of FireCCIS310, this vegetation index was replaced by the NBR2 derived from the SYN SWIR bands. The NBR2 is characterised by a sharp drop after a fire event, leading to low post-fire values (Roteta et al., 2021). It is known for providing high separability between burned and unburned areas, as well as homogeneity within the burned patches, which is an important factor to detect the entire patch (Liu et al., 2021; Roteta et al., 2019).

To obtain the separability for a given day (*t*) and pixel at location (*x, y*), 16 days with valid observations were needed: eight from the days previous to *t* (pre-timeframe) and eight from the days after *t* (post-timeframe). In both temporal directions, the selected days had to be the closest in time from *t* and, hence, the minimum searching window was of eight days (i.e. from *t*-8 to *t*-1 for the pre-timeframe and from *t* to *t* + 7 for the post-timeframe). This initial window was progressively changed

by −1 in the case of the pre-timeframe and + 1 in the case of the post-timeframe until eight days with valid observation were found for each of the timeframes. The maximum searching window was of 30 days to ensure that the statistics represented the short-term pre- and post-fire scenarios. If eight valid observations were not found in either of the two timeframes a pixel was labelled as 'non-observed'. This value of eight showed a good balance between a representative estimation of the statistics and the number of non-observed areas (Giglio et al., 2018). Two summary statistics were computed for the pre- and post-timeframe, using in each case the corresponding eight NBR2 values: the 10% trimmed mean ($NBR2_{pre}(t,x,y)$ and $NBR2_{post}(t,x,y)$) and trimmed standard deviation ($\sigma_{pre}(t,x,y)$ and $\sigma_{post}(t,x,y)$). When the number of values is proportional to 10, the 10% trimmed summary statistics exclude the corresponding proportion of the lowest and highest values, e.g. with 10 values the lowest and highest values are excluded leaving eight values to compute the statistic. However, when the number of values is not
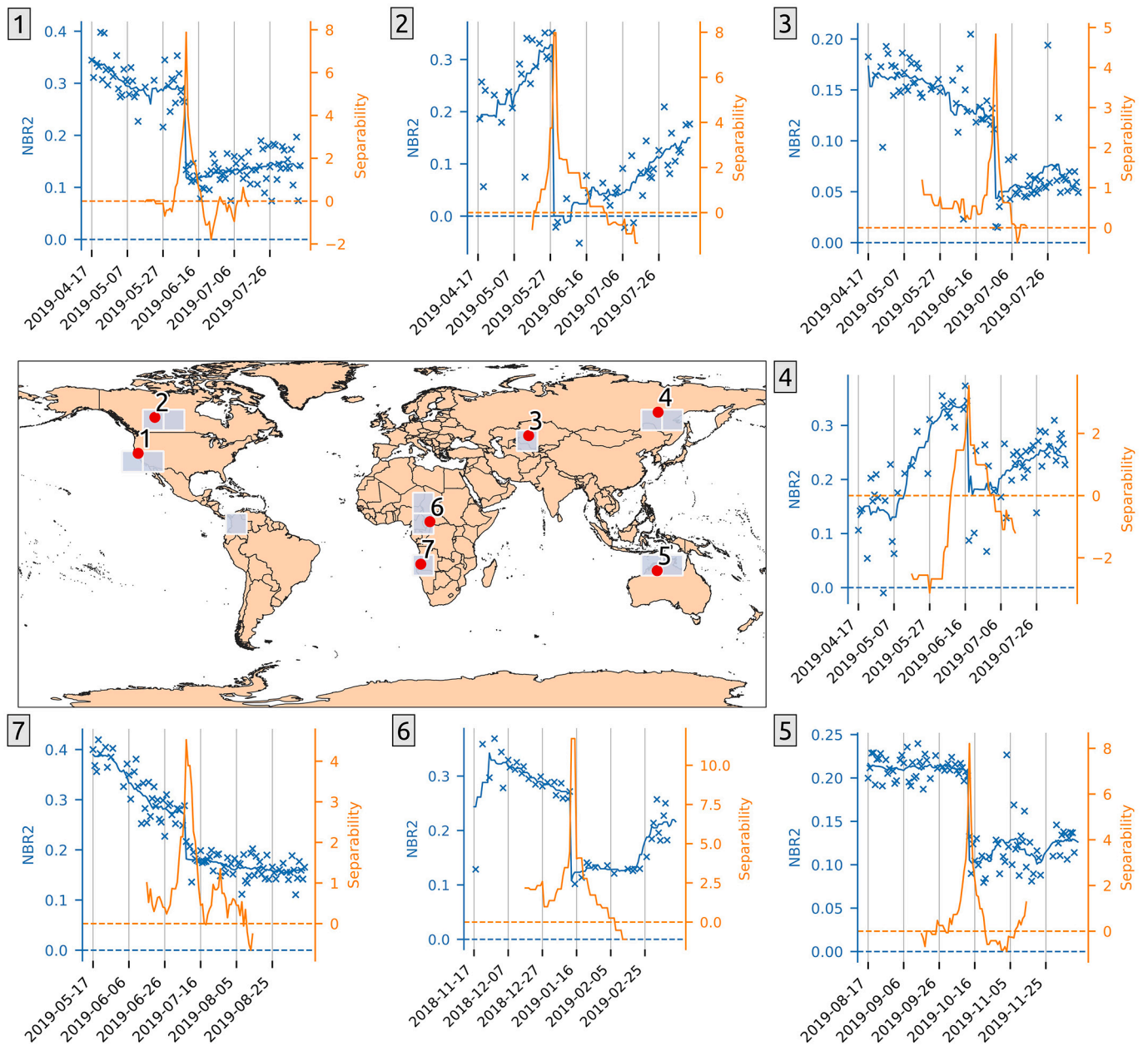

Fig. 3. NBR2 vegetation index and the derived separability *S* through different burned pixels distributed along the calibration tiles. In all cases, an active fire was detected in the same location within 0–1 days difference. The locations belong to the following biomes: Mediterranean (1), boreal forest (2, 4), deserts & xeric shrubland (3), and tropical savanna (5, 6, 7).

proportional to 10, weights have to be estimated for each value. In our case, the lowest and highest values were weighted by a factor of 0.2 and the rest by a factor of 1. Finally, the separability for the day t and pixel x, y was computed as shown in Eq. (1).

Fig. 3 shows the behaviour of both the NBR2 and S for several burned locations distributed among the calibration areas. A sharp drop in the NBR2, such as those expected to be generated by fires, leads to large positive values of S. Therefore, monthly composites were generated by maximising S. To avoid to artificially split fires that took place at the end or beginning of a month, the monthly composites were generated considering S values of the last 15 days of the previous month (m-1), the days of the month (m) being processed, and the first 15 days of the following month (m + 1). Using these data, the day with the maximum separability was selected for each pixel ($t_{max}(m,x,y)$). The separability ($S_{max}(m,x,y)$) and the change in NBR2 ($\Delta NBR2_{max}(m,x,y)$) of $t_{max}(m,x,y)$ were stored as well. Fig. 4b, c, and d show an example of each of these monthly composites of September 2019 for a region located in Angola.

Since burned patches were expected to have a high temporal coherence in t_{max} an additional variable, denoted as $\sigma_{t,max}(m,x,y)$, was computed (Giglio et al., 2009). This variable was characterised by the standard deviation of t_{max} within a rook's case window (3 × 3), i.e. pixels at the diagonals were not considered, around each pixel. To avoid the loss of fine (i.e. 1-pixel) sections of burned patches an edge-restoring ranked order filter that selects the 33rd percentile within a 3 × 3 window around the pixel was applied (Astola and Kuosmanen, 1997) (Fig. 4e).

2.5. Generation of active fire clusters

Following the FireCCI51 algorithm (Lizundia-Loiola et al., 2020), FireCCIS310 used spatio-temporal active fire clusters (STC) to guide the thresholding process. Each cluster was assumed to represent a fire and, hence, dynamic thresholds for each burned patch were computed by defining cluster-adapted burned and unburned samples (Section 2.8).

Clusters were created considering the spatial and temporal distribution of the active fires. The spatial distance, also known as area of influence (R_{AI}), proposed by Lizundia-Loiola et al. (2020) to consider two active fires part of the same cluster was of 1875 m. However, this distance was obtained based on MODIS active fires and was suited for its spatial resolution of 1 km. Therefore, considering the higher spatial resolution of VIIRS active fires used by the new algorithm, the R_{AI} distance was adapted based on the proportionality of the spatial resolutions of VIIRS and MODIS active fires: 375 m / 1000 m * 1875 m = 703.125 m. This adjusted distance was more adequate to address the much higher density of active fires per burned patch that can be found in VIIRS 375 m in comparison to MODIS (Oliva and Schroeder, 2015; Schroeder et al., 2014; Waigl et al., 2017). Regarding the temporal difference to consider two active fires part of the same cluster, the original threshold of 4 days proposed by Lizundia-Loiola et al. (2020) was kept since it was related to the characteristics of the fire regimes and not to the sensor's characteristics. Fig. 4a shows an example of these STC, where different colours represent different clusters. To increase the overlap between consecutive months, active fires of the last 5 days of the previous month and the first 5 days of the following month were used along with the active fires of the month being processed.

2.6. Selection of potential active fires (PAF)

As explained in the input data section, the VIIRS thermal anomalies product used by the new algorithm provided a "type" field that allows applying an initial filtering of presumed vegetation fires. It might be reasonable to think that due to the low commission rates of active fire products (Schroeder et al., 2014), further filtering was not necessary. However, several key points must be considered when using active fires for burned area mapping. The first and main limitation is set by the spatial resolution of the sensor that is providing the spectral information for burned area detection. In this case, the average SYN pixel was about 300 m, meaning that the smallest burned area that can be detected comprises one that causes a discernible change in spectral reflectance at 300 m resolution, nominally 90,000 m^2. Conversely, a fire burning at
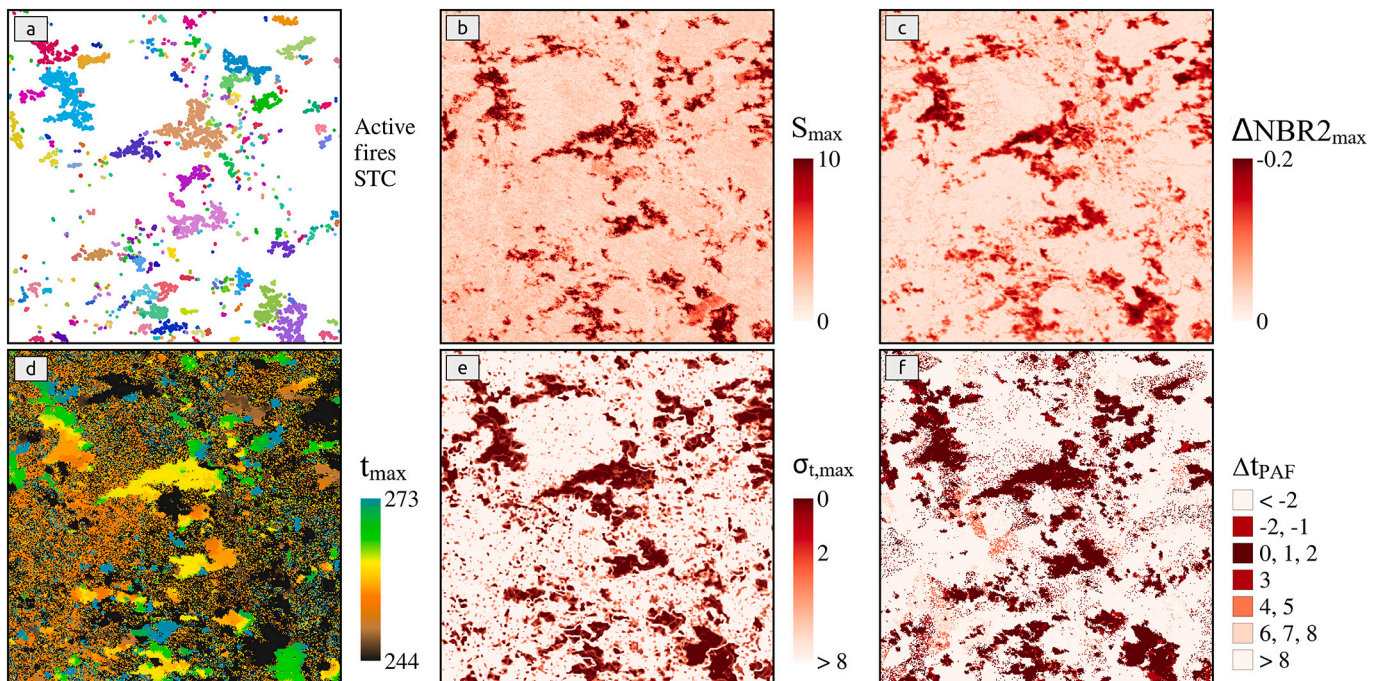

Fig. 4. Monthly variables used by the burned area mapping algorithm: a) active fires spatio-temporal clusters (STC), b) maximum separability (S_{max}), c) change in NBR2 of the day with the maximum separability ($\Delta NBR2_{max}$), d) day with the maximum separability (t_{max}), e) temporal coherence of the day with the maximum separability ($\sigma_{t,max}$), and f) difference between the day with the maximum separability and the day of detection of the nearest Potential Active Fire (Δt_{PAF}). The example belongs to September 2019 for an area centred at 18.9°E, 16.7°S in Angola (Africa). Colours in a) just indicate different STC.

around 650 K with an area of 50 m^2 (night-time case) or 250 m^2 (day-time case) had a 50% probability of being detected by the VIIRS active fire algorithm (see probability curves as a function of fire area and temperature in Schroeder et al. (2014)). This contrast between detection capabilities made highly probable that fires correctly identified by VIIRS were not able to generate a detectable spectral change in SYN at 300 m resolution. Additionally, it could happen that the "type" field provided by the active fire product was not able to properly classify all thermal sources that were not related to vegetation fires (volcanos, static sources, etc.).

Before applying any further filtering process, active fires were relocated in the pixel with the maximum $S_{max}(m,x,y)$ within a 3 × 3 window around the pixel that fell just below the original location of the active fire. The maximum separability location (x',y') was assumed to better represent the actual position of the active fire instead of the original location (x,y) since the high radiative energy released by the fire might contaminate surrounding pixels. Then, for each relocated active fire, the difference between $t_{max}(m,x,y)$ and the date of the active fire, defined as $t_f(m,x',y')$, was computed $(\Delta t_f(m,x',y'))$. The potential active fires (PAF) were selected from the relocated active fires based on the following set of rules:

1. $S_{max}(m,x',y') \geq 2$
2. Either one of the following conditions was met:
   a. $(-2 \leq \Delta t_f(m,x',y') \leq 8)$ AND $(\sigma_{t,max}(m,x',y') \leq 1)$
   b. $(0 \leq \Delta t_f(m,x',y') \leq 2)$ AND $(\sigma_{t,max}(m,x',y') \leq 8)$

These conditions enhanced three fundamental aspects that pixels with a high probability of being burned should met. First, the separability S_{max} must be high (condition 1), pointing out a substantial spectral change. Second, temporal agreement between the day with the maximum separability and the day when the active fire was detected should be high ($\Delta t_f(m,x',y')$ in conditions 2a and 2b). And third, the spatial correlation of the day when the spectral change was detected should be high among adjacent pixels ($\sigma_{t,max}(m,x',y')$ in conditions 2a and 2b). As a result, PAF represented not only pixels with a high probability of being burned, but also pixels that were part of burned patches that were able to generate a spectral change at 300 m.

The global parameter $S_{max} \geq 2$ was set based on the distribution derived from 66,186 locations defined by active fires that had an associated burned patch in the reference perimeters. In the cases of texture ($\sigma_{t,max}$) and day difference (Δt_f and Δt_{PAF}) two ranges were defined based on the same calibration set: a first range of values where the probability of burn was higher (>60% of the active fires fall in this range) ($\sigma_{t,max} \leq 1$ or $0 \leq \Delta t_f \leq 2$) and a second less restrictive range that was used to confirm the burn ($\sigma_{t,max} \leq 8$ or $-2 \leq \Delta t_f \leq 8$). Fig. 5 shows the

distributions and the selected thresholds for each of these variables.

2.7. A priori burned patches

At this point, the $\Delta t_f(m,x',y')$ variable, which provided valuable information to quantify the temporal uncertainty, was extended to the whole tile. To do that, the $t_f(m,x'y')$ of the nearest PAF was assigned to each pixel of the image based on Thiessen polygons (Brassel and Reif, 1979), obtaining $t_{PAF}(m,x,y)$. Then, $\Delta t_{PAF}(m,x,y)$ was calculated as the difference between $t_{max}(m,x,y)$ and $t_{PAF}(m,x,y)$ (Fig. 4f). To define a priori burned patches a contextual growing was applied, iteratively adding pixels that met the following conditions:

1. An adjacent pixel in a rook's case window (3 × 3) must be a PAF or a pixel previously identified as part of an a priori burned patch
2. $S_{max}(m,x,y) \geq 2$
3. Either one of the following conditions must be met:
   a. $(-2 \leq \Delta t_{PAF}(m,x,y) \leq 8)$ AND $(\sigma_{t,max}(m,x,y) \leq 1)$
   b. $(0 \leq \Delta t_{PAF}(m,x,y) \leq 2)$ AND $(\sigma_{t,max}(m,x,y) \leq 8)$

These conditions were the same used to select PAF, but replacing $\Delta t_f(m,x',y')$ by $\Delta t_{PAF}(m,x,y)$, so they could be extended to the whole tile. At this step, a rook's case window, which did not consider pixels located in the diagonals, was used as it is more restrictive than a queen's case window (i.e. where diagonals are considered).

2.8. Establishing cluster-adapted thresholds

2.8.1. Definition of training samples

Due to the availability of high-resolution active fires data from VIIRS, the definition of a suitable burned sample was more feasible than the definition of the unburned sample. As it was already mentioned, active fire products showed low commission errors while providing accurate positioning and timing of the fire events (Boschetti et al., 2010). Therefore, most of the hybrid algorithms used for burned area detection rely on those locations and their surroundings to define the burned samples (Alonso-Canas and Chuvieco, 2015; Chuvieco et al., 2018; Giglio et al., 2018; Giglio et al., 2009; Lizundia-Loiola et al., 2020). In the case of the unburned class, however, it is much more difficult to define a sample due to its spectral heterogeneity. A common approach is to consider as unburned those pixels located further than a given distance from active fires (Alonso-Canas and Chuvieco, 2015; Chuvieco et al., 2018; Lizundia-Loiola et al., 2020).

In our case, training samples were defined for each STC (Fig. 6a) to estimate cluster-adapted thresholds, properly expressing local conditions. To define what "local" meant, first, the a priori burned patch
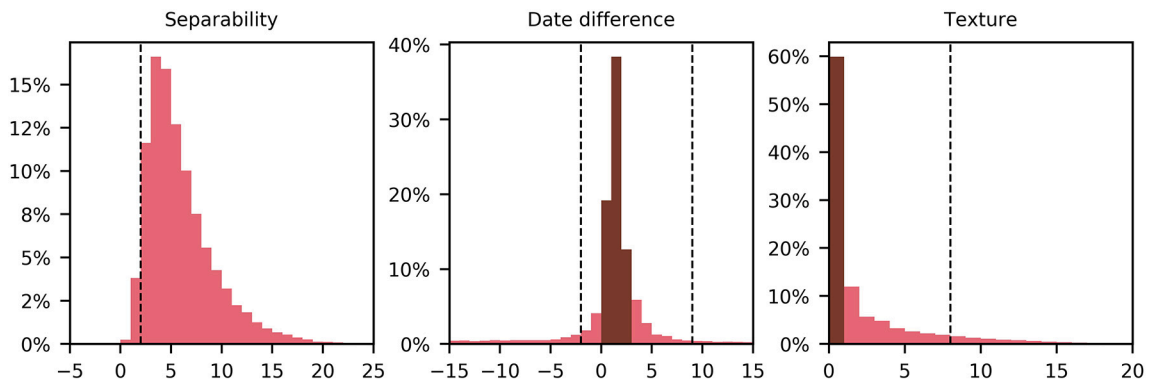
Fig. 5. Distribution of the maximum separability (S_{max}), maximum separability day vs. active fire day difference (Δt_f), and texture ($\sigma_{t,max}$) variables derived from 66,186 locations defined by active fires that had an associated burned patch in the reference perimeters. The dashed lines show the global thresholds selected to guide the algorithm. The dark red areas show the regions of the variable where the probability of burn was higher. (For interpretation of the references to colour in this figure legend, the reader is referred to the web version of this article.)

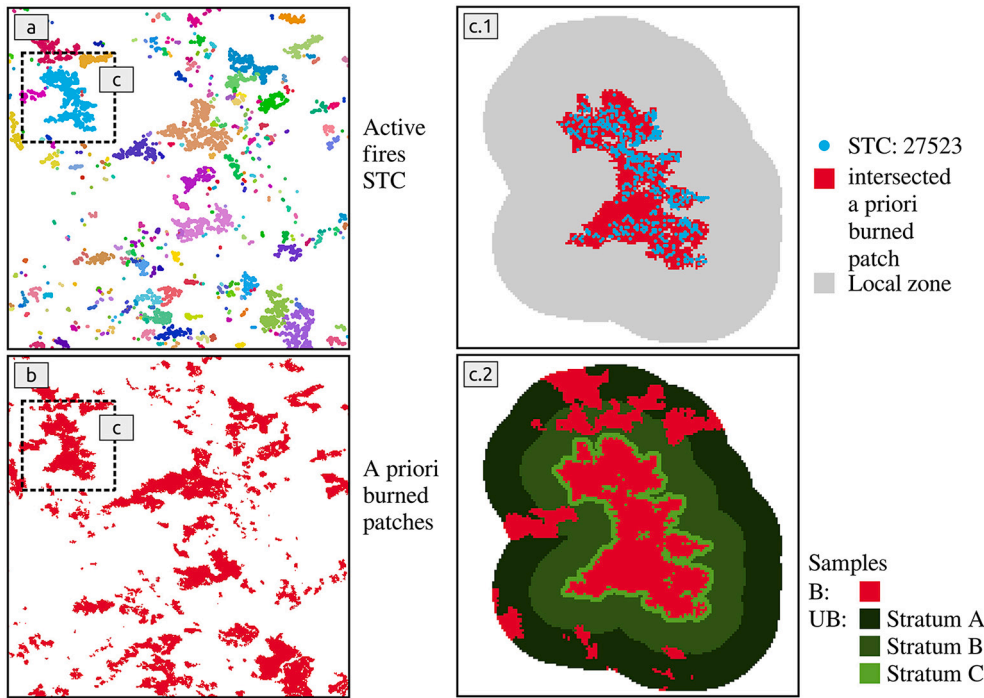**Fig. 6.** Definition of the burned (B) and unburned (UB) samples for the active fires cluster (STC) number 27523 located at 18.5°E, 16.5°S (Angola) of September 2019. In c.1 the local zone is defined by a buffer of 10 km around the border of the a priori burned patch intersected by the STC 27523. In c.2, stratum A, B, and C correspond to distances between 10 and 5 km, 5 km and R_{AI} (i.e. the distance used to create the clusters), and less than R_{AI}, respectively. Colours in a) just indicate different STC.

(Fig. 6b) that was intersected by the PAF of a given STC was selected. Then, a buffer of 10 km was defined from the border of the intersected a priori burned patch, defining thus the local zone (Fig. 6 c.1). The burned sample, labelled as $B(m,STC)$, was composed of pixels that fall within that local zone and belong to any a priori burned patch. The remaining pixels represented the unburned class ($UB(m,STC)$). Fig. 6 shows an example of the samples that were selected for a fire at 18.5°E, 16.5°S in September 2019, where in c.2 red areas represent $B(m,STC)$ and green tones $UB(m,STC)$. This cluster-based sampling methodology allowed representing local conditions and adapting to different fire regimes that might be present throughout the tile without the need of other auxiliary data (e.g. land cover data) (Lizundia-Loiola et al., 2020).

2.8.2. Threshold calculation

Obtaining adequate thresholds is crucial for burned area mapping algorithms that rely on contextual growing to detect burned patches. Too restrictive thresholds reduce commission errors, but at the expense of incomplete detections of burned patches. Conversely, too relaxed thresholds may reduce omission errors but at the cost of excessive growing and, hence, more commission errors (Alonso-Canas and Chuvieco, 2015; Giglio et al., 2009). The FireCCIS310 algorithm used an automatic threshold methodology, called Otsu threshold (Otsu, 1979), to achieve cluster-adapted thresholds. The Otsu method is a non-parametric thresholding approach that does not need any control parameter and maximizes the separability between two classes based on a gray-level histogram. Basically, the optimum threshold is the one with the minimum intra-class variance and the maximum inter-class variance. Otsu thresholding is a technique that has been widely used in burned area mapping studies (Amos et al., 2019; Bin et al., 2019; Otón et al., 2021; Roteta et al., 2021).

Before applying the Otsu method and considering the rationale behind it, it was necessary to balance $B(m,STC)$ and $UB(m,STC)$ samples to generate a training sample where each of the classes had the same proportion (50%). In the case of the burned sample all the pixels from $B(m,STC)$ were included, while for the unburned class a selection was carried out since the size of $UB(m,STC)$ was, in most cases, greater than $B(m,STC)$. Therefore, a subsample of $UB(m,STC)$, denoted as $ub(m,STC)$, was selected based on a stratified random sampling approach. Three

strata were defined based on the distance to the nearest $B(m,STC)$ pixel: stratum A covered from 10 to 5 km, stratum B covered from 5 km to R_{AI} (i.e. the distance used to construct the STC), and stratum C encompassed pixels closer than R_{AI} (Fig. 6 c.2). The subsample was, whenever possible, randomly selected from stratum A. If this stratum did not provide enough pixels, the remaining pixels were randomly selected from stratum B, and so on. The Otsu method was applied to the resultant training sample: $B(m,STC) \cup ub(m,STC)$. To ensure the representativeness of the heterogeneity of $UB(m,STC)$ and, hence, of the threshold ($TH(m,STC)$), this procedure was repeated 500 times. The high number of repetitions ensured a good representation of the normal distribution of $TH(m,STC)$ and, for that reason, $TH(m,STC)$ was computed as the average of all the thresholds:

$$TH(m, STC) = \frac{1}{500} \sum_{k=1}^{500} TH_k(m, STC)(B(m, STC) \cup ub_k(m, STC)) \quad (3)$$

The thresholding process was only applied to the $\Delta NBR2_{max}$ variable. Considering the properties of the NBR2, i.e. high separability between burned and unburned areas as well as homogeneity within the burned patches, it was considered the most suitable variable over which to apply the contextual growing process described in Section 2.10.

2.9. Estimation of the threshold surface

As a result of the previous step an adapted threshold of the $\Delta NBR2_{max}$ variable was obtained for each STC of the tile and month being processed ($TH(m,STC)$). To avoid any anomaly that might derive from the thresholding process and considering the similarity that should be expected among the thresholds of STC spatially close to each other, $TH(m, STC)$ were combined to obtain the threshold surface ($TH_S(m,x,y)$) (Fig. 7). To do that, for every pixel in the tile the weighted average of all the different $TH(m,STC)$ within a 20 km radius was computed. The weight was determined by the number of PAF of each STC, assuming that the higher the number of PAF, the larger the size of $B(m,STC)$ and the more representative the $TH(m,STC)$.

Finally, all initial relocated active fires, not just PAF, were compared against the corresponding threshold in $TH_S(m,x,y)$. Active fires whose $\Delta NBR2_{max}(m,x',y') < TH_S(m,x',y')$, which meant a greater spectral
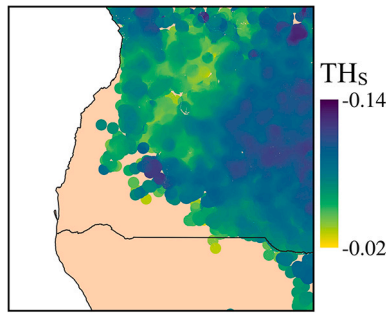
Fig. 7. Threshold surface (TH_S) of the $\Delta NBR2_{max}$ variable generated for the 10° x 10° tile, which encompassed the area between 10°-20° E and 10°-20° S, corresponding to September 2019.

change, were considered as seeds for the posterior contextual growing step. In those occasional cases in which a given PAF did not pass that test, the a priori burned patch that contained the PAF was directly considered as burned in the final burned map, finalising the classification process for that specific PAF.

2.10. Generation of the final burned area map

In the final step of the algorithm a contextual growing, which added pixels in an iterative process, was applied to fully detect burned patches and, hence, reduce omission errors. Seeds were used as starting points for the contextual growing, using their corresponding threshold determined by $TH_S(m,x',y')$ as stopping criteria, which was fundamental for an efficient growing process (Zhang et al., 2005). A pixel was detected as burned if the following conditions were met:

1. An adjacent pixel in a queen's case window (3×3) must be a seed or a pixel previously identified as burned
2. $\Delta NBR2_{max}(m,x,y) < TH_S(m,x',y')$
3. $S_{max}(m,x,y) \geq 2$
4. $\sigma_{t,max}(m,x,y) \leq 8$

where (x,y) represented the location of the pixel being considered and (x',y') represented the location of the seed from which the growing process started. To avoid problems derived from excessive growing a patch-based filtering process proposed by Lizundia-Loiola et al. (2020) was applied:

F1. Patches with a quotient between their total number of burned pixels and seeds over 1000 were removed.

F2. Patches with a quotient between the number of burned pixels located closer than the area of influence (R_{AI}) from the seeds and their total number of burned pixels below 0.1 (10%) were removed.

F3. Contiguous patches to burned patches were removed if they did not contain active fires and were connected by a 1-pixel width connection to the actual burned patch. This last filter avoided cases where burned areas were falsely connected to unburned areas with high NBR2 changes.

2.11. Uncertainty characterization

Uncertainty characterization of Earth Observation data has been increasingly required by the scientific community of climate and atmosphere modellers. However, both standard approaches proposed by the Joint Committee for Guides in Metrology (2008a, b) fail to provide an appropriate uncertainty propagation framework for FireCCIS310, because analytical methods are not feasible in the case of threshold-based categorisation algorithms (Merchant et al., 2017), and Monte Carlo simulations of large datasets require huge computational resources.

In this study, uncertainty was simulated using a clustering approach,

which generated a look-up table (LUT) of representative spatiotemporal patterns derived from four predictive variables used by the burned area mapping algorithm ($\Delta NBR2_{max}$, S_{max}, $\sigma_{t,max}$ and Δt_{PAF}). First, *K-means* was used to generate clusters over the entire dataset. Then, predictive variables of these clusters were overlaid with the reference dataset (Section 2.12.1) to characterize each pixel by a set of six variables, i.e. the aforementioned four predictive variables, the pixel classification (burned: B or unburned: UB) in the reference data, and the pixel classification in FireCCIS310.

The confusion matrices of that set of representative patterns allowed computing the probability of burn of each pixel depending on its classification (B or UB). The probability of burn of pixels that were classified as burned was computed using the precision index whereas the false omission rate was used for pixels classified as unburned. The former expressed the proportion of correct positive prediction (TP) within the pattern (the negative ones are denoted as TN), while the latter indicated the proportion of false negative predictions (FN, false positives FP). The two probabilities were estimated as:

$$P_B = \frac{TP}{TP + FP} * 100 \tag{4}$$

$$P_{UB} = \frac{FN}{TN + FN} * 100 \tag{5}$$

where P_B denotes the probability of burn of pixels classified as burned by FireCCIS310, and P_{UB} denotes the probability of burn of pixels classified as unburned.

2.12. Accuracy assessment

2.12.1. Spatial validation

The spatial accuracy of the FireCCIS310 burned area map was assessed by comparison with reference data obtained from Landsat 8 images. For this purpose, we used the reference data collection 'C3S_global_2017_2019' recently released as part of the Burned Area Reference Database (Franquesa et al., 2020b). This reference dataset comprises 316 reference files that can be used to validate global burned area products for the years 2017 to 2019. The 105 reference files corresponding to the sampling year 2019 were selected to validate the FireCCIS310 burned area product. These reference files were produced for sampling units that were selected following a stratified sampling design, allowing us to compute unbiased estimators of accuracy and their associated uncertainties. To produce this reference dataset, population units were defined based on the Thiessen Scene Areas (TSAs) of the Landsat WRS-2 frames, which allow for a non-overlapping partitioning of the Earth's surface. Sampling units were stratified across eight biomes according to the Ecoregion 2017 map (Dinerstein et al., 2017) and further stratification was applied based on the burned area extent of the FireCCI51 burned area product. The strata allocation of the 105 sample units was carried out considering the contribution of each stratum to the total burned area (Padilla et al., 2017), hence, a greater number of sample units were assigned to those strata with greater fire activity. Then, fire perimeters were extracted from Landsat 8 time series for each sample unit to produce long temporal reference units, which include three class categories: burned, unburned and unobserved. To extract the reference perimeters, the centre of each Landsat scene (100 km × 100 km) was visually interpreted to train a supervised classification algorithm (Random Forest) implemented in the Google Earth Engine platform (Roteta et al., 2021). A detailed description of the methods and characteristics of the 'C3S_global_2017_2019' dataset can be found in Franquesa et al. (2022).

The metrics used to assess the FireCCIS310 product accuracy were the omission error (*Oe*), commission error (*Ce*), the dice coefficient (*DC*) (Dice, 1945), which combines the metrics *Oe* and *Ce* in a single measure, and the relative bias (*relB*), which informs whether a product under- or overestimates the burned area. The reference files were used to obtain

the error matrices from which to estimate these global accuracy metrics and their standard errors, following the methodology described in Franquesa et al. (2022).

2.12.2. Temporal reporting accuracy validation

The temporal reporting accuracy refers to how accurately the burned area algorithms can assign the actual day of burn to the pixels detected as such. To assess this accuracy global burned area products are typically compared with active fires (Boschetti et al., 2010; Campagnolo et al., 2019). Since we validated global burned area products that used either MODIS or VIIRS active fires as input, the temporal reporting accuracy was validated based on almost 1.7 million MODIS active fires (MCD14ML product) and almost 8 million active fires from VIIRS (VNP14IMGML product) of the year 2019.

2.13. Intercomparison with existing products

One of our main objectives when developing the new burned area algorithm was to provide an alternative to MODIS-data-based algorithms. It was important, therefore, to make an intercomparison against the publicly available MODIS burned area products MCD64A1 c6 (Giglio et al., 2018), FireCCI51 (Lizundia-Loiola et al., 2020) and C3SBA11 (Lizundia-Loiola et al., 2021). The idea was to check if burned area patterns followed a similar spatial distribution. To do that, burned area was aggregated at biome level based on the same Ecoregion 2017 map used in the stratification of the validation process.

3. Results

3.1. Accuracy assessment

3.1.1. Spatial validation

Global accuracy estimates and the corresponding standard errors (shown in parenthesis in the tables and through the text) of FireCCIS310 for the year 2019 are shown in Table 1, along with the equivalent global accuracy estimates extracted from Franquesa et al. (2022) for C3SBA11, FireCCI51, and MCD64A1 c6. The new algorithm was the most accurate in terms of *DC*, *Oe*, and *relB*, while MCD64A1 c6 showed the lowest *Ce*. The global *DC* of FireCCIS310 was 68.1% (±2.5), being 6.4%, 4.2%, and 8.3% higher than C3SBA11, FireCCI51, and MCD64A1 c6, respectively (comparisons were expressed in absolute terms for accuracy metrics). *Oe* was 5.3% lower for FireCCIS310 than for FireCCI51, the second product with the lowest *Oe*. *Ce* was the only accuracy metric where the FireCCIS310 product did not provide the most accurate results, although the differences were less relevant than for *Oe*, with all products ranging between 17.5 and 20.8%. In all products *relB* had negative values, meaning an underestimation of burned area and being the closest to zero for FireCCIS310.

Biome level accuracy metrics followed a similar pattern (Table 2). FireCCIS310 was the most accurate product in terms of *DC* for all biomes, although different patterns were observed for *Ce* and *Oe*. Boreal forest showed the highest accuracies for all products, where *DC* values ranged from 75.7% (±4.5%) to 82.2% (±1.2%). Conversely, tropical forest had the highest *Ce* and *Oe*, although it was the biome where

Table 1

Global error estimates [%] for the three products and year 2019, with the standard error in parenthesis. Data for C3SBA11, FireCCI51, and MCD64A1 c6 was extracted from Table 5 of Franquesa et al. (2022). In bold is the product that shows the highest accuracy in each specific metric.

	C3SBA11	FireCCI51	MCD64A1 c6	FireCCIS310
DC	61.7 (2.9)	63.9 (2.8)	59.8 (3.2)	**68.1 (2.5)**
Ce	18.6 (1.7)	20.8 (1.7)	**17.5 (1.4)**	19.2 (1.7)
Oe	50.3 (3.4)	46.5 (3.4)	53.1 (3.6)	**41.2 (3.0)**
relB	−39.0 (3.5)	−32.5 (3.4)	−43.1 (3.8)	**−27.2 (2.7)**

Table 2

Estimated error metrics [%] at biome level for each product and year 2019, with the standard error in parenthesis. The total BA mapped in the reference data (BAref) is provided per biome in km^2. Data for C3SBA11, FireCCI51, and MCD64A1 c6 was extracted from Table 6 of Franquesa et al. (2022). In bold is the product that shows the highest accuracy in each specific metric.

Biome		C3SBA11	FireCCI51	MCD64A1 c6	FireCCIS310
Boreal forest	DC	76.7 (1.7)	79.0 (1.6)	75.7 (4.5)	**82.2 (1.2)**
	Ce	24.2 (6.1)	23.2 (3.3)	**20.4 (2.2)**	21.4 (4.0)
	Oe	22.3 (5.5)	18.8 (1.9)	27.8 (6.9)	**14.0 (2.5)**
	relB	**2.5 (14.9)**	5.7 (5.9)	−9.3 (7.1)	9.4 (8.5)
	BAref	1840.8			
Deserts & xeric shrublands	DC	52.8 (7.7)	52.5 (7.7)	75.5 (2.5)	**76.7 (2.6)**
	Ce	15.5 (1.9)	20.1 (0.9)	19.1 (1.5)	**15.1 (0.8)**
	Oe	61.6 (8.0)	60.9 (8.4)	**29.2 (4.6)**	30.1 (4.8)
	relB	−54.6 (9.0)	−51.0 (10.1)	**−12.4 (6.3)**	−17.6 (6.3)
	BAref	439.0			
Mediterranean	DC	57.3 (2.7)	69.5 (6.2)	74.5 (6.4)	**83.4 (4.7)**
	Ce	28.8 (4.4)	23.7 (6.9)	**13.2 (1.7)**	17.0 (1.8)
	Oe	52.1 (1.8)	36.2 (5.6)	34.7 (8.8)	**16.2 (7.6)**
	relB	−32.7 (1.6)	−16.3 (0.7)	−24.8 (8.8)	**1.0 (7.2)**
	BAref	283.6			
Temperate forest	DC	62.6 (10.0)	59.6 (9.8)	51.5 (10.1)	**67.5 (10.4)**
	Ce	**17.0 (7.2)**	22.3 (10.4)	19.6 (8.8)	21.5 (12.6)
	Oe	49.7 (10.3)	51.7 (9.0)	62.1 (9.0)	**40.9 (9.0)**
	relB	−39.4 (7.4)	−37.8 (4.7)	−52.9 (6.3)	**−24.7 (2.9)**
	BAref	889.1			
Temperate savanna	DC	64.2 (1.9)	62.0 (1.9)	55.0 (1.9)	**67.6 (2.0)**
	Ce	19.2 (1.0)	19.6 (1.6)	21.9 (2.1)	**17.9 (0.9)**
	Oe	46.8 (2.5)	49.6 (2.4)	57.6 (2.3)	**42.6 (2.6)**
	relB	−34.2 (3.3)	−37.3 (3.0)	−45.7 (3.4)	**−30.1 (2.8)**
	BAref	3403.1			
Tropical forest	DC	46.3 (8.2)	50.7 (8.0)	42.6 (8.4)	**57.8 (6.6)**
	Ce	24.1 (6.7)	24.1 (6.1)	**20.6 (4.7)**	27.6 (5.4)
	Oe	66.7 (7.4)	61.9 (7.7)	70.9 (7.3)	**51.9 (7.1)**
	relB	−56.1 (7.1)	−49.8 (7.3)	−63.4 (7.6)	**−33.6 (6.3)**
	BAref	19,204.3			
Tropical savanna	DC	67.0 (3.1)	68.9 (2.9)	66.3 (3.4)	**72.0 (2.5)**
	Ce	16.3 (1.5)	19.4 (1.7)	16.0 (1.5)	**15.5 (1.3)**
	Oe	44.1 (3.9)	39.9 (3.8)	45.2 (4.2)	**37.2 (3.2)**
	relB	−33.2 (4.1)	**−25.4 (4.0)**	−34.8 (4.5)	−25.7 (3.1)
	BAref	104,793.3			
Tundra	DC	78.8 (3.1)	69.9 (9.3)	50.9 (10.7)	**81.8 (0.9)**
	Ce	18.9 (1.9)	26.9 (12.7)	26.0 (15.9)	**11.8 (5.7)**
	Oe	**23.4 (7.5)**	33.1 (6.4)	61.2 (9.4)	23.7 (3.1)

Table 2 (*continued*)

Biome		C3SBA11	FireCCI51	MCD64A1 c6	FireCCIS310
	relB	−5.5 (11.5)	−8.6 (7.1)	−47.6 (10.8)	−13.4 (9.0)
	BAref	564.9			

FireCCIS310 provided the greatest improvement over FireCCI51 in terms of *Oe* (10% lower). In the case of deserts & xeric shrublands the two products that used SWIR region (FireCCIS310 and MCD64A1 c6) clearly outperformed those based only on NIR (C3SBA11 and FireCCI51).

3.1.2. Temporal reporting accuracy validation

Table 3 and Table A1 show global and per biome temporal reporting accuracy estimates for the four global burned area products, while Fig. 8 shows the distribution per biome of the differences between the date of detection provided by the algorithms and the corresponding active fire detection date. In the case of the estimates of Table 3 and Table A1 the differences were counted in absolute terms, i.e. number of days before (negative) or after (positive) the date of the active fire. All the mentioned figure and tables provide the temporal reporting accuracy estimated from MODIS active fires. Additionally, Fig. A1 presents the same distribution as Fig. 8 but based on VIIRS active fires.

The most accurate product in terms of temporal reporting accuracy was MCD64A1 c6, followed by FireCCIS310. The former product detected 56.5% of the cases within 0–1 days difference globally, while the latter was able to detect 53.0% of the cases. Conversely, C3SBA11 and FireCCI51 labelled only 21.2% and 18.0% of the cases within the same difference, respectively, less than a half of the other two products. FireCCIS310 progressively reduced the difference with MCD64A1 c6 from 3.5% for a 0–1 difference to 0.8% for a 0–10 day difference (comparisons were expressed in absolute terms). Both C3SBA11 and FireCCI51 showed a clear trend to detect burned area after the fire, more specifically within the first 10 days after the active fire. The four products show similar accuracies within 0–10 day difference.

A similar pattern was observed at biome level, where MCD64A1 c6 was the most accurate product in most of the biomes. It is worth noting that the difference in temporal reporting accuracy between MCD64A1 c6 and FireCCIS310 substantially reduced from 0 to 1 to 0–3 days difference, e.g. in deserts and xeric shrubland it was reduced from 10.9% to 2.6% and from 10.1% to 2.6% in the case of the Mediterranean biome. FireCCIS310 outperformed the temporal reporting accuracy of the Copernicus and FireCCI products, detecting, on average, 33.4% more cases within 0–1 days difference per biome.

The analysis based on VIIRS raised practically the same figures confirming all the patterns among products (Fig. A1).

3.2. Intercomparison with existing BA products

FireCCIS310 was globally processed for the year 2019 and, hence, all the figures and tables refer to that year. Fig. 9 shows the spatial distribution of the global burned area detected by the new algorithm at 1° pixels. Table 4 shows the annual burned area (km^2) and the relative differences (%) between FireCCIS310 and the rest of the products for each biome and globally. Fig. 10 gives an overview of the relative contribution of each biome to the global discrepancy between the product presented in this paper and the rest, as well as between the number of active fires detected by VIIRS and MODIS. Complementary, Fig. 11, Fig. A2, and Fig. A3 represent, also at 1°, the spatial distribution of the quotients resulted from the division between the burned area of FireCCIS310 and FireCCI51, MCD64A1 c6, and C3SBA11, respectively.

The new FireCCIS310 algorithm detected 4.99×10^6 km^2 globally for the year 2019 (Table 4). Most of the burned area was concentrated in the tropical savanna biome (3.31×10^6 km^2), mainly in the northern and southern hemisphere Africa, but with substantial contributions from Los Llanos in Colombia and Venezuela, the Cerrado in Brazil, and northern Australia. Tropical forests of Southeast Asia showed a high fire activity as well, being the primary source of burned area for that biome. A high fire activity spot was noticeable in agricultural areas of Punjab and Haryana in northwest India. A second belt of burned area completely crossed Eurasia around the 50° N latitude line, encompassing deserts and xeric grasslands and shrublands of Kazakhstan, and temperate savanna and forest regions. For this latter biome another relevant contributor was the east coast of Australia, as the summer of 2019 implied an extreme fire season (Bowman et al., 2020). Complementary, boreal forests were affected by fire activity as well, especially those located in Alaska and Far East Russia.

The new product detected 37.3%, 27.4%, and 43.7% more burned area than C3SBA11, FireCCI51, and MCD64A1 c6, respectively (Table 4). The highest difference was for tropical forest where FireC-CIS310 more than doubled the burned area detected by the other three products, i.e. between 0.46 and 0.50×10^6 km^2 more burned area. Something similar happened with deserts and xeric shrublands between FireCCIS310 and C3SBA11 and FireCCI51, but not for MCD64A1 c6. Conversely, C3SBA11, FireCCI51 and FireCCIS310 detected practically the same amount of burned area for boreal forest and tundra, being slightly higher for the former. In general terms, the new algorithm detected much more burned area in most of the biomes, reaching up to 1.36×10^6 km^2 more burned area in comparison to C3SBA11, 1.07×10^6 km^2 compared to FireCCI51 and 1.52×10^6 km^2 in comparison to MCD64A1 c6.

From those more than one million km^2 of difference among the FireCCIS310 product and the other global burned area products, around 80% came from tropical forests and tropical savanna, which represented on average 85% of the global burned area for the year 2019 according to the four products. These same biomes contributed in a similar way (81.4%) to the global discrepancy found between the number of active fires detected by VIIRS and MODIS, where the former detected 13 million more active fires. In general, apart from deserts & xeric shrublands and boreal forest, the increase in the annual burned area by the FireCCIS310 product in each biome was consistent with an increase in the active fire detections of VIIRS.

The spatial distribution of the discrepancies within each biome followed a similar pattern when FireCCIS310 was compared to FireCCI51 (Fig. 11), MCD64A1 (Fig. A2), and C3SBA11 (Fig. A3). In the case of tropical savanna, the increase was homogeneously distributed through the biome and pixels showed differences of less than two times (x2) the burned area of the other product. A similar pattern was observed in temperate forests and savannas of Central Asia for C3SBA11 and Fire-CCI51, but not for MCD64A1 c6 which presented high discrepancies (> x5) in comparison to FireCCIS310. Tropical forest concentrated most of the global pixels where FireCCIS310 detected >5 times (> x5) the area of the other products. Examples of these sharp increase can be found in Central America, Perú, Amazon River estuary, Democratic Republic of the Congo, Indonesia, and Southeast Asia. In this last region, a clear border effect was noticeable when comparing the new product against C3SBA11 and FireCCI51, which is a consequence of the border effect
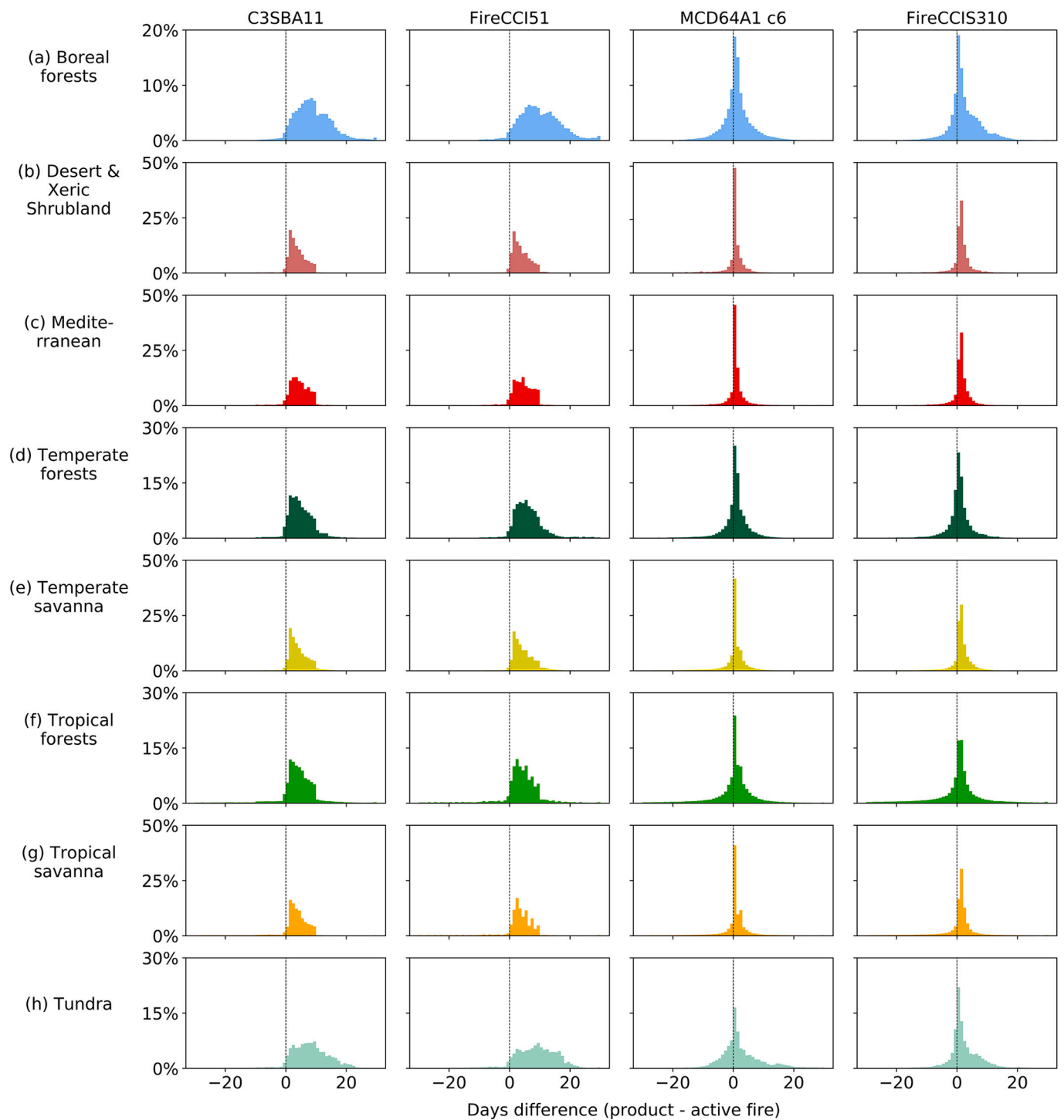
Table 3

Global temporal reporting accuracy for each product and year 2019 compared to MODIS active fires. The differences were accounted for in absolute terms, e.g. either if the difference is −1 (the product detected the fire one day before the active fire) or + 1 (the product detected the fire one day after the active fire) the difference is considered to fall in the 0–1 days frame. In bold is the product that shows the highest accuracy in each specific timeframe.

	C3SBA11	FireCCI51	MCD64A1 c6	FireCCIS310
0–1 days	21.2%	18.0%	**56.5%**	53.0%
0–3 days	47.4%	46.0%	**78.8%**	76.7%
0–5 days	67.4%	66.9%	**87.2%**	85.3%
0–10 days	93.9%	92.6%	**96.2%**	95.4%

Fig. 8. Temporal reporting accuracy for each product and biome compared to MODIS active fires. Each bin of the histograms represents a 1-day step.

originally present in these products (Liu and Crowley, 2021; Lizundia-Loiola et al., 2021). Additionally, except for the MCD64A1 c6 product, substantial differences (> x3) were found in deserts and xeric shrublands of Australia, in line with the abovementioned sharp burned area increase of FireCCIS310 over C3SBA11 and FireCCI51 (Table 4).

4. Discussion

This paper presents a new global burned area algorithm, called FireCCIS310, based on S3 SYN 300 m spectral information and VIIRS 375 m active fires. As the MODIS mission approaches its end, suitable

replacements will be needed to ensure the provision of global burned area maps at moderate spatial resolution in the coming years and with the Copernicus Programme promising 20+ years it is reasonable to develop a suitable product for the equivalent Copernicus S3 sensor. The new global burned area algorithms should achieve similar or even higher spatial and temporal accuracies in comparison to their predecessors, while overcoming as much as possible the limitations found by the fire community in the last years in different burned area products (Chuvieco et al., 2019). The new algorithm represents a step forward in some of these aspects.

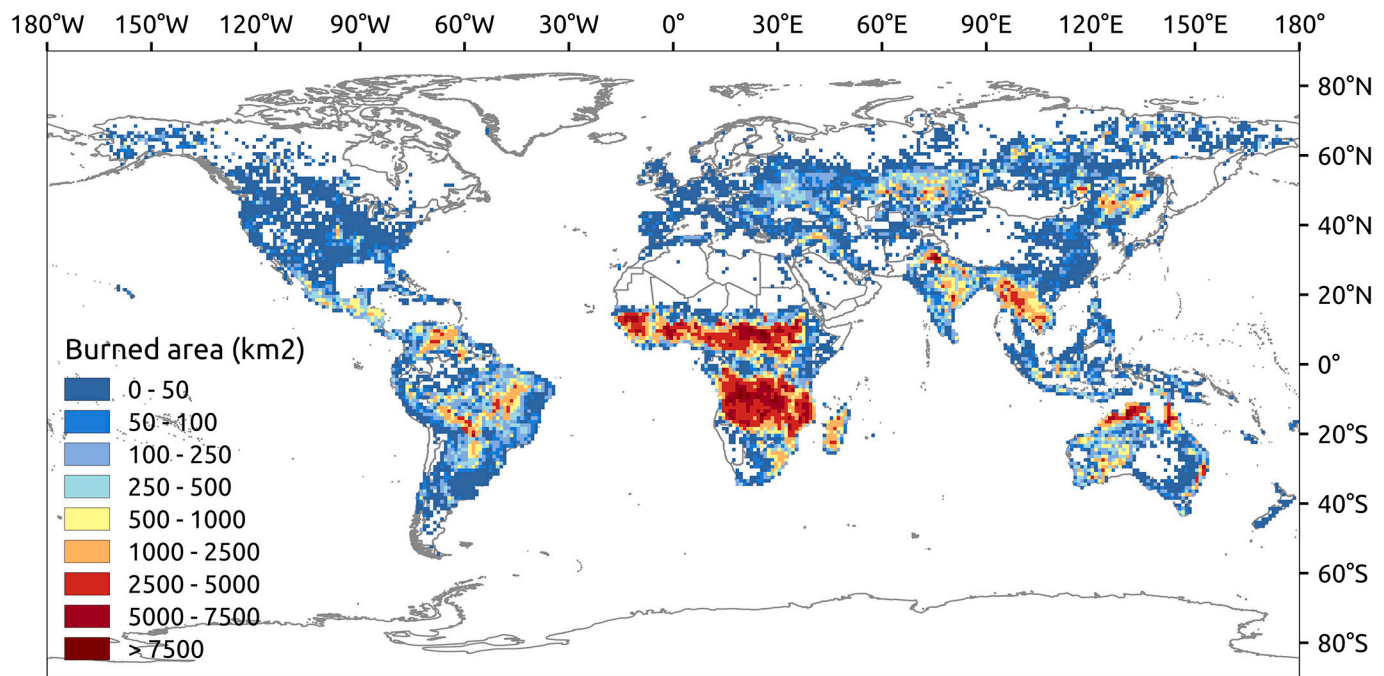FireCCIS310 used a novel surface reflectance product, which had not

Fig. 9. Burned area (km^2) of the year 2019 detected by the FireCCIS310 product at 1° spatial resolution.

Table 4
Burned area (km^2) per product and the relative difference (%) between FireCCIS310 and the other burned area products for the year 2019 and each biome.

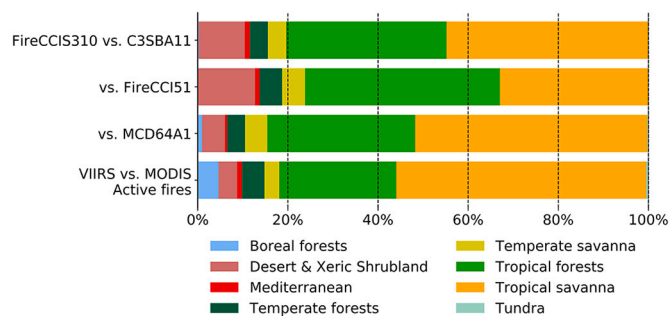|	Burned area (km^2)				FireCCIS310 vs.		
	C3SBA11	FireCCI51	MCD64A1 c6	FireCCIS310	C3SBA11	FireCCI51	MCD64A1 c6
Boreal forest	90,503	86,711	72,370	87,145	−3.9%	+0.5%	+20.4%
Deserts & xeric shrublands	113,707	116,907	176,164	253,192	+122.7%	+116.6%	+43.7%
Mediterranean	24,975	29,162	32,364	39,765	+59.2%	+36.4%	+22.9%
Temperate forest	110,884	111,999	105,320	165,621	+49.4%	+47.9%	+57.3%
Temperate savanna	164,995	165,610	145,221	220,141	+33.4%	+32.9%	+51.6%
Tropical forest	411,926	433,493	400,165	897,703	+117.9%	+107.1%	+124.3%
Tropical savanna	2,701,210	2,958,452	2,529,860	3,311,552	+22.6%	+11.9%	+30.9%
Tundra	13,044	11,531	8437	12,000	−8.7%	+4.1%	+42.2%
Global	3,631,243	3,913,865	3,469,901	4,987,119	+37.3%	+27.4%	+43.7%

Fig. 10. Relative contribution of each biome to the annual burned area differences found between FireCCIS310 and C3SBA11, FireCCI51, and MCD64A1 c6 for the year 2019. The bar in the bottom shows the same but regarding the difference in the number of active fires detected by VIIRS and MODIS.

previously been used for burned area mapping, which combines measurements of OLCI and SLSTR sensors to provide daily, global coverage of Vis, NIR and SWIR spectral bands at 300 m spatial resolution. Until now, moderate resolution global burned area mapping algorithms had to decide between using sensors that provided lower spatial resolution but wider spectral capabilities (MCD64A1 c6: Giglio et al. (2018)) or higher spatial resolution but lower spectral capabilities (C3SBA11: Lizundia-

Loiola et al. (2021); FireCCI51: Lizundia-Loiola et al. (2020)). The S3 SYN product partially avoids this issue by providing SWIR bands at 300 m. The burned signal after the fire persists for a longer time in vegetation indices that include the SWIR spectral region (Melchiorre and Boschetti, 2018), making them more sensitive for burned area mapping. This persistency in the spectral change is crucial for the development and application of multi-temporal indices that take full advantage of daily images. In that sense, FireCCIS310 proposed a modified version of a multi-temporal separability index (Giglio et al., 2009) by using the NBR2, a vegetation index based on short and long SWIR highly sensitive to burned area (Roteta et al., 2019). This allowed to generate monthly composites that were more stable than those used by previous FireCCI versions, which had been generated by selecting reflectance of a single day (Alonso-Canas and Chuvieco, 2015; Chuvieco et al., 2018; Lizundia-Loiola et al., 2020).

Another important novelty of the algorithm in comparison to previous FireCCI products was the use of global parameters when selecting potentially burned pixels from the locations of input active fires. In that sense, the use of VIIRS active fires at 375 m supposed a new challenge, because, although the commission errors were expected to be low (Schroeder et al., 2014), the active fire product was expected to detect cooler and smaller fires as well as achieve higher densities per burned patch compared to MODIS active fire detections (Schroeder et al., 2014). In fact, Oliva and Schroeder (2015) found that VIIRS active fires offered
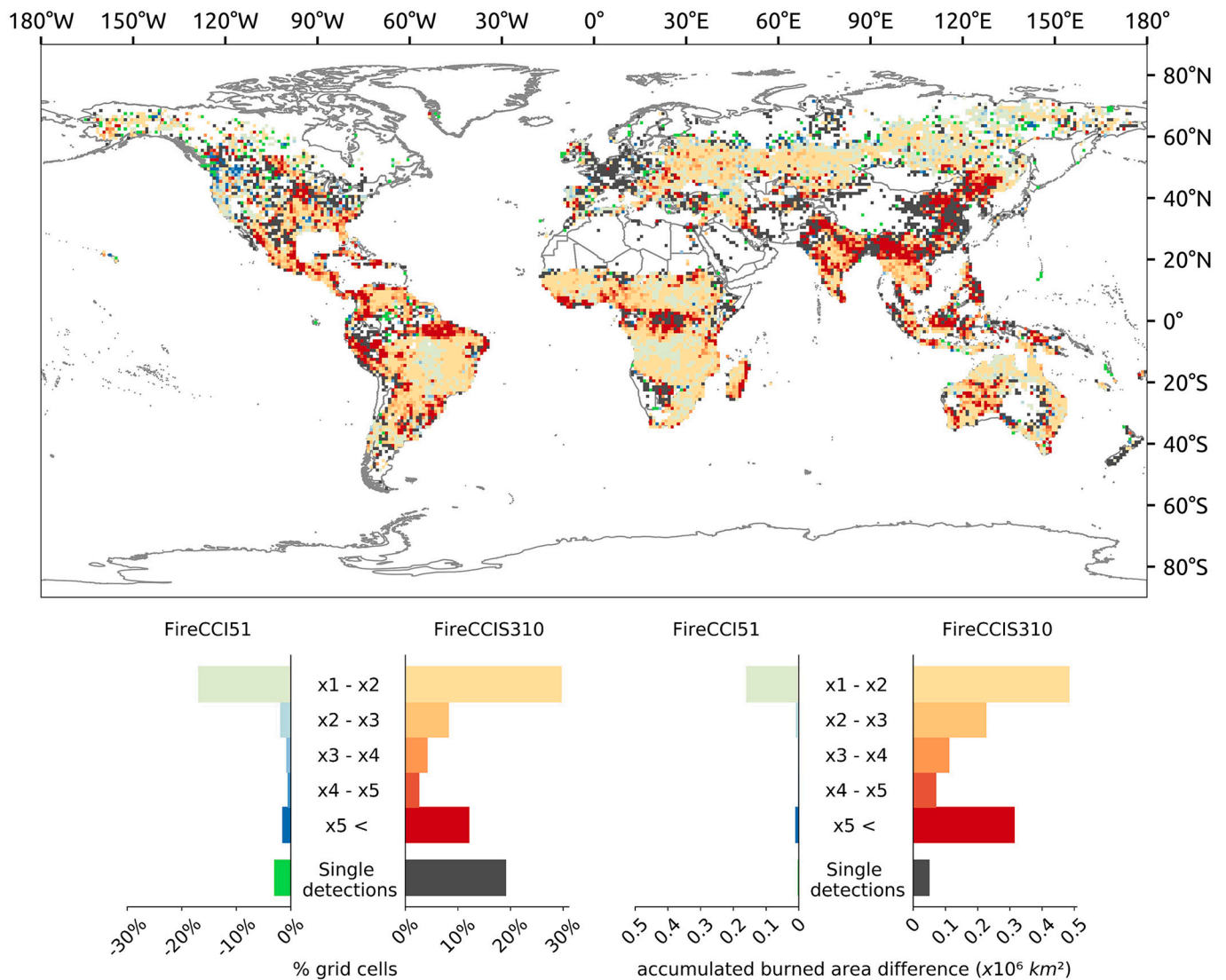
Fig. 11. Spatial distribution of the differences between the annual burned areas of the FireCCI51 and FireCCIS310 products at 1° spatial resolution. Each grid cell shows the quotient resulted from dividing the burned area of the product that detected the most by the one that detected the least. Thus, xN represents how many times more burned area was detected, being N the quotient. The red tones represent grid cells where FireCCIS310 detected more than FireCCI51, while the blue ones represent the contrary. The single detections are those cases where only one of the products detected burned area. (For interpretation of the references to colour in this figure legend, the reader is referred to the web version of this article.)

enhanced capabilities in terms of related and independent omission errors. The VIIRS 375 m active fire product detected 13 million more fires than MODIS in 2019. However, this enhanced capacity of the VIIRS product to detect smaller fires increased the presence of SYN 300 m pixels with negligible spectral changes because the fire covered a reduced proportion of the pixel. For that reason, the algorithm had to be able in an initial step to filter those cases to avoid contamination of the thresholding process. It must be pointed as well that the use in that step of tile-level thresholds, which changed from one tile to another, was found to be the source of the border effects in previous FireCCI products and also in C3SBA11, which followed a similar approach (Liu and Crowley, 2021; Lizundia-Loiola et al., 2021). Instead, the new algorithm defined global thresholds based on the distribution shown by the VIIRS active fires that had an associated reference perimeter, leading to a consistent potentially burned pixel selection. Fig. 12 shows the area reported by Liu and Crowley (2021) in northwest India as an example of the border effects of FireCCI51, which have now been removed.

In terms of burned area detection thresholds, the use of spatio-temporal active fire clusters proposed by Lizundia-Loiola et al. (2020)

to obtain thresholds that better adjust to the internal variability within a tile had proved to be a good alternative to those approaches that use additional auxiliary data with the same objective. However, the same study underlined that the definition of cluster-based samples should be improved, especially for those burned patches with a low active fire density. For example, to determine the unburned samples FireCCI51 used the distance from active fires as a criterion rather than the border of a priori burned patches, as it is done by FireCCIS310. This led to the contamination of the unburned sample in those cases where burned pixels were far away (> 10 km) from the nearest active fire (e.g. fires of fast spread in deserts & xeric shrublands). Besides, the fixed linear relation between the burned and unburned sample used by FireCCI51 to estimate the thresholds was replaced by the Otsu thresholding, which is designed to dynamically find the optimum threshold between two expected classes within a distribution (Roteta et al., 2021).

The combination of improved input data and detection capabilities made FireCCIS310 the most accurate among the compared products in terms of *DC*, *Oe*, and *relB*. In the case of *Ce*, the new algorithm slightly improved FireCCI51. However, in general terms, the four products
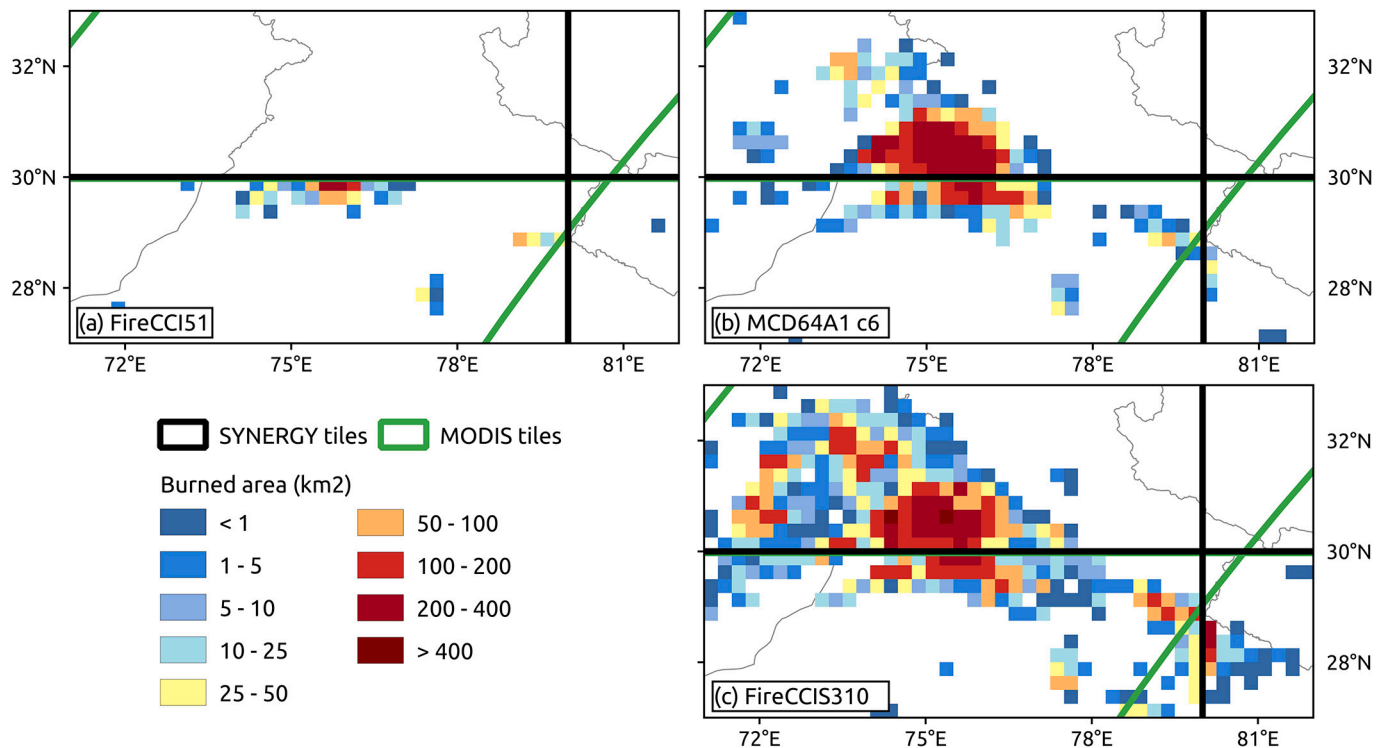
Fig. 12. Example of the area reported by Liu and Crowley (2021) as a clear example of tiling artifacts in FireCCI51 in November 2019 in northwest India. Both MCD64A1 c6 and FireCCIS310 did not show such artifacts. The border at 30°N is the same for MODIS and SYN tiles.

might already be near the maximum achievable *Ce* considering the impacts of the coarse spatial resolution (Franquesa et al., 2022). It is well known that global burned area products suffer from a systematic underestimation (Boschetti et al., 2019; Chuvieco et al., 2018; Franquesa et al., 2022), particularly caused by small fires (Ramo et al., 2021; Randerson et al., 2012). Our SYN-based product also presented omission problems, but to a lesser extent than for other existing burned area products, while maintaining similar levels of commission errors. The relative bias was therefore improved. Results at biome level suggested good detection capabilities across different fire regimes. Nevertheless, the per-biome accuracy analysis should be interpreted with caution due to the small sample size allocated in some biomes (Franquesa et al., 2022).

Another substantial improvement of FireCCIS310 in comparison with its precursors was the temporal reporting accuracy. Both C3SBA11 and FireCCI51 are known to have low temporal reporting accuracy, as a result of the compositing criteria, with only high detection rates for the first 10 days after the fire (Lizundia-Loiola et al., 2021; Lizundia-Loiola et al., 2020). Instead, the multi-temporal separability index used by FireCCIS310, which considered eight pre- and eight post-fire NBR2 daily values, allowed for a more robust estimation of the day of the fire. FireCCIS310 showed a narrow distribution around the 0–1 differences, accounting for >50% of the detections, similar to MCD64A1 c6.

Regarding global burned area, FireCCIS310 drastically increased the estimations for the year 2019, with around 1 million km^2 more detected burned area than FireCCI51, the second product with the highest estimations (4.99 versus 3.91 × 10^6 km^2, respectively). Most of this increase (around 80%) was observed in tropical forest and tropical savanna, which accounted for 0.46, and 0.35 × 10^6 km^2 of the global difference, respectively. In that sense, the use of VIIRS 375 m active fires instead of MODIS 1 km played a key role. After all, every burned patch detected by FireCCIS310 must contain at least one active fire and, hence, any reduction in *Oe* of the original active fire product had the potential to be translated, although not fully, into the *Oe* of the burned area product. This context explained the general increase in global burned area

estimates and, specifically, in those biomes with a high proportion of small fires (< 100 ha) (Ramo et al., 2021; Randerson et al., 2012), although a more in-depth analysis is required to assess the performance of the new algorithm in relation to fire size (Campagnolo et al., 2021). Conversely, boreal forest was the only biome where an increase in active fire detections between VIIRS and MODIS did not imply an increase in burned area, which could be reasonable since the large size, high energy and low spread-rates of the fires in this biome ensure active fire detections per burned patch. The deserts and xeric shrubland biome was a clear example in which the use of the SWIR spectral bands benefited FireCCIS310 and MCD64A1 c6 since NIR was expected to have weaker signal in burnings of dry vegetation (Campagnolo et al., 2021; Jacques et al., 2014; Miettinen, 2007).

The results presented in this study suggest that the use of VIIRS 375 m active fires had important implications for burned area mapping algorithms, but also for the fire community. The increased capability of detecting burned area, and the improved spatial and temporal accuracies, implied benefits for applications such as greenhouse emission modeling (van der Werf et al., 2017) or individual fire patches detection (Andela et al., 2019; Laurent et al., 2018). However, these same positive characteristics could become an issue for those users that need long time-series of burned area. The generation of long-time records requires combining products derived from different input datasets that must be consistent to avoid hindering temporal trends (Lizundia-Loiola et al., 2021). While the use of VIIRS 375 m active fires seemed to make FireCCIS310 less consistent with MODIS-based products, the algorithm was designed to ingest any active fire products, hence, coarser resolution active fire products might bring greater correlation with existing BA products. For example, VIIRS active fires at 750 m or even SLSTR active fires at 1 km may lead to global burned area products more similar to MODIS ones (Schroeder et al., 2014; Xu et al., 2021), but this decision would probably lead to a reduction in the spatial accuracy. Future studies should therefore analyse how the jump between products based on MODIS, SLSTR and VIIRS active fires could be properly reconciled to build consistent time series of burned area.

5. Conclusions

This paper has described a new burned area algorithm adapted to Sentinel-3 SYN and VIIRS active fires data to generate a global burned area product independent of MODIS data, with similar or better accuracies in terms of spatial and temporal detection. As MODIS is coming to the end of its operating life, alternative sources of Earth observation data are critical to extend the available time series of burned area information to the next decades. We tested our algorithm with a global processing for the year 2019 of a new synthetic product (SYN) that includes reflectance at 300 m resolution of the two sensors (OLCI and SLSTR) on board Copernicus Sentinel-3 A and B satellites plus VIIRS 375 m active fires. Comparison of our results with existing products in the same year showed consistent spatial trends, but higher detection rates in the new product, named FireCCIS310. In fact, this product detects 27% more burned area than its precursor, FireCCI51. This increase was mainly related to the higher sensitivity of VIIRS 375 m to detect smaller and/or cooler fires than MODIS, as well as the use of SWIR bands included in the SYN data, particularly in detecting burned areas in regions of sparse vegetation. The resulting burned area product is part of the ESA FireCCI project and is publicly available. Semi-operational production of this algorithm is expected in the next few years within the FireCCI project extension.

Data availability

The FireCCIS310 dataset is freely available in both grid and pixel format through the CCI Open Data Portal (https://climate.esa.int/es/odp/#/dashboard, last accessed on July 2022). Additionally, the reference perimeter files used for the global spatial validation of the FireCCIS310 product are publicly available at https://doi.org/10.21950/BBQQU7 (last accessed on July 2022) (Franquesa et al., 2020a).

CRediT authorship contribution statement

Joshua Lizundia-Loiola: Conceptualization, Methodology, Formal analysis, Investigation, Data curation, Writing – original draft, Software, Writing – review & editing. **Magí Franquesa:** Writing – original draft, Software, Writing – review & editing. **Amin Khairoun:** Methodology, Writing – original draft, Software, Writing – review & editing. **Emilio Chuvieco:** Writing – original draft, Writing – review & editing, Supervision, Project administration, Funding acquisition.

Declaration of Competing Interest

The authors declare that they have no conflict of interest.

Data availability

Data is available through the CCI Open Data Portal

Appendix A

Table A1

Temporal reporting accuracy for each product and biome for the year 2019 compared to MODIS active fires. The differences were accounted in absolute terms, e.g. either if the difference is −1 (the product detected the fire one day before the active fire) or +1 (the product detected the fire one day after the active fire) the difference is considered to fall in the 0–1 days frame. In bold is the product that shows the highest accuracy in each specific biome and time-frame.

Biome		C3SBA11	FireCCI51	MCD64A1 c6	FireCCIS310
Boreal forest	0–1 days	8.2%	6.9%	**44.4%**	42.3%
	0–3 days	19.6%	16.7%	**68.9%**	63.5%
	0–5 days	33.0%	28.7%	**81.5%**	76.0%
	0–10 days	68.6%	60.1%	**95.7%**	92.9%
Deserts & xeric shrublands	0–1 days	28.7%	30.2%	**71.5%**	60.6%
	0–3 days	57.6%	57.6%	**87.2%**	84.6%
	0–5 days	77.2%	76.2%	**93.1%**	91.1%
	0–10 days	98.8%	98.0%	**98.4%**	97.7%
Mediterranean	0–1 days	18.6%	20.3%	**70.9%**	60.8%
	0–3 days	45.5%	43.1%	**86.7%**	84.1%
	0–5 days	67.8%	66.0%	92.1%	**92.3%**
	0–10 days	98.4%	98.2%	97.8%	**98.3%**
Temperate forest	0–1 days	21.1%	13.2%	53.9%	**54.8%**
	0–3 days	44.5%	33.5%	77.0%	**78.5%**
	0–5 days	63.8%	54.3%	88.0%	**88.1%**
	0–10 days	93.4%	89.0%	**97.9%**	97.7%
Temperate savanna	0–1 days	25.9%	24.2%	**62.9%**	59.1%
	0–3 days	54.4%	51.3%	**83.1%**	81.8%
	0–5 days	73.2%	70.4%	90.3%	**90.8%**
	0–10 days	96.9%	94.6%	97.8%	**98.0%**
Tropical forest	0–1 days	20.9%	19.0%	45.0%	**46.2%**
	0–3 days	44.8%	43.6%	**70.3%**	69.5%
	0–5 days	65.4%	65.0%	**82.2%**	80.0%
	0–10 days	94.4%	93.4%	**95.4%**	93.5%
Tropical savanna	0–1 days	23.2%	19.1%	**60.1%**	55.7%
	0–3 days	52.6%	51.4%	**82.0%**	80.0%
	0–5 days	73.9%	73.8%	**88.9%**	87.4%
	0–10 days	98.2%	97.7%	**96.2%**	95.8%

Table A1 (*continued*)

Biome		C3SBA11	FireCCI51	MCD64A1 c6	FireCCIS310
Tundra	0–1 days	10.5%	8.9%	35.1%	**46.4%**
	0–3 days	23.1%	20.1%	57.1%	**66.4%**
	0–5 days	36.0%	30.4%	71.0%	**77.3%**
	0–10 days	70.7%	61.7%	89.8%	**94.4%**
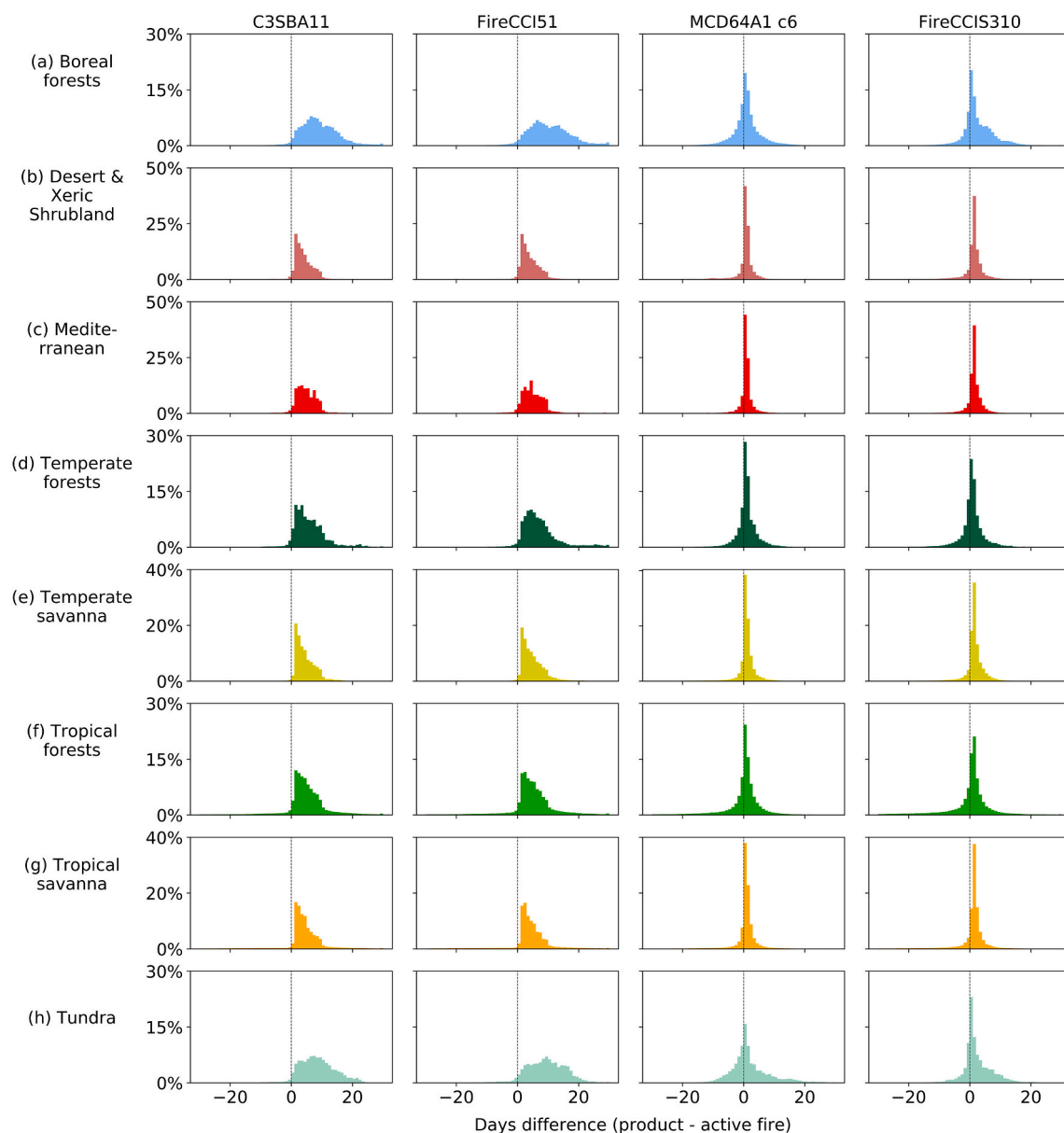
Fig. A1. Temporal reporting accuracy for each product and biome compared to VIIRS active fires. Each bin of the histograms represents a 1-day step.
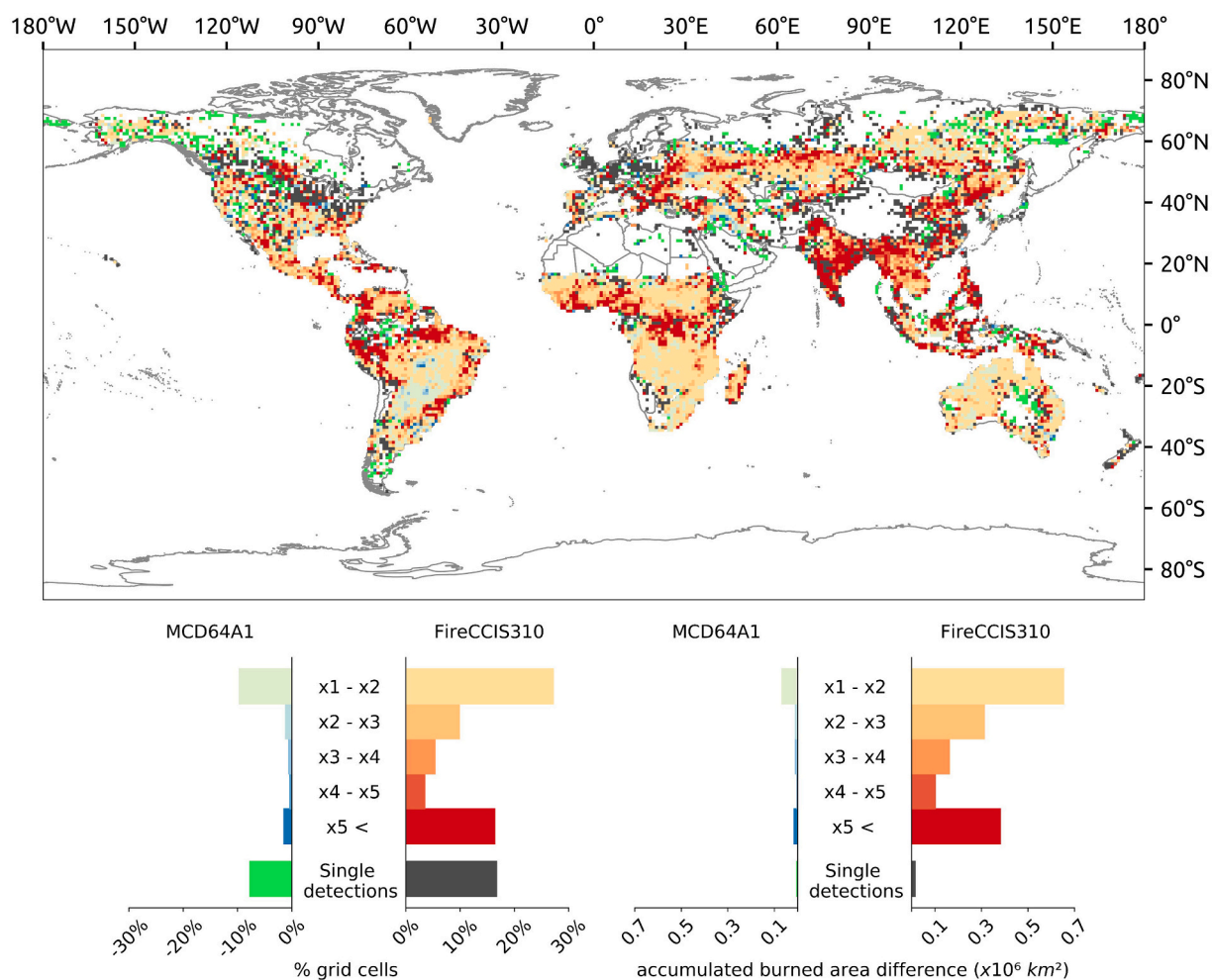
Fig. A2. Spatial distribution of the differences between the annual burned areas of the MCD64A1 c6 and FireCCIS310 products at 1° spatial resolution. Each grid cell shows the quotient resulted from dividing the burned area of the product that detected the most by the one that detected the least. Thus, xN represents how many times more burned area was detected, being N the quotient. The red tones represent grid cells where FireCCIS310 detected more than MCD64A1 c6, while the blue ones represent the contrary. The single detections are those cases where only one of the products detected burned area. (For interpretation of the references to colour in this figure legend, the reader is referred to the web version of this article.)
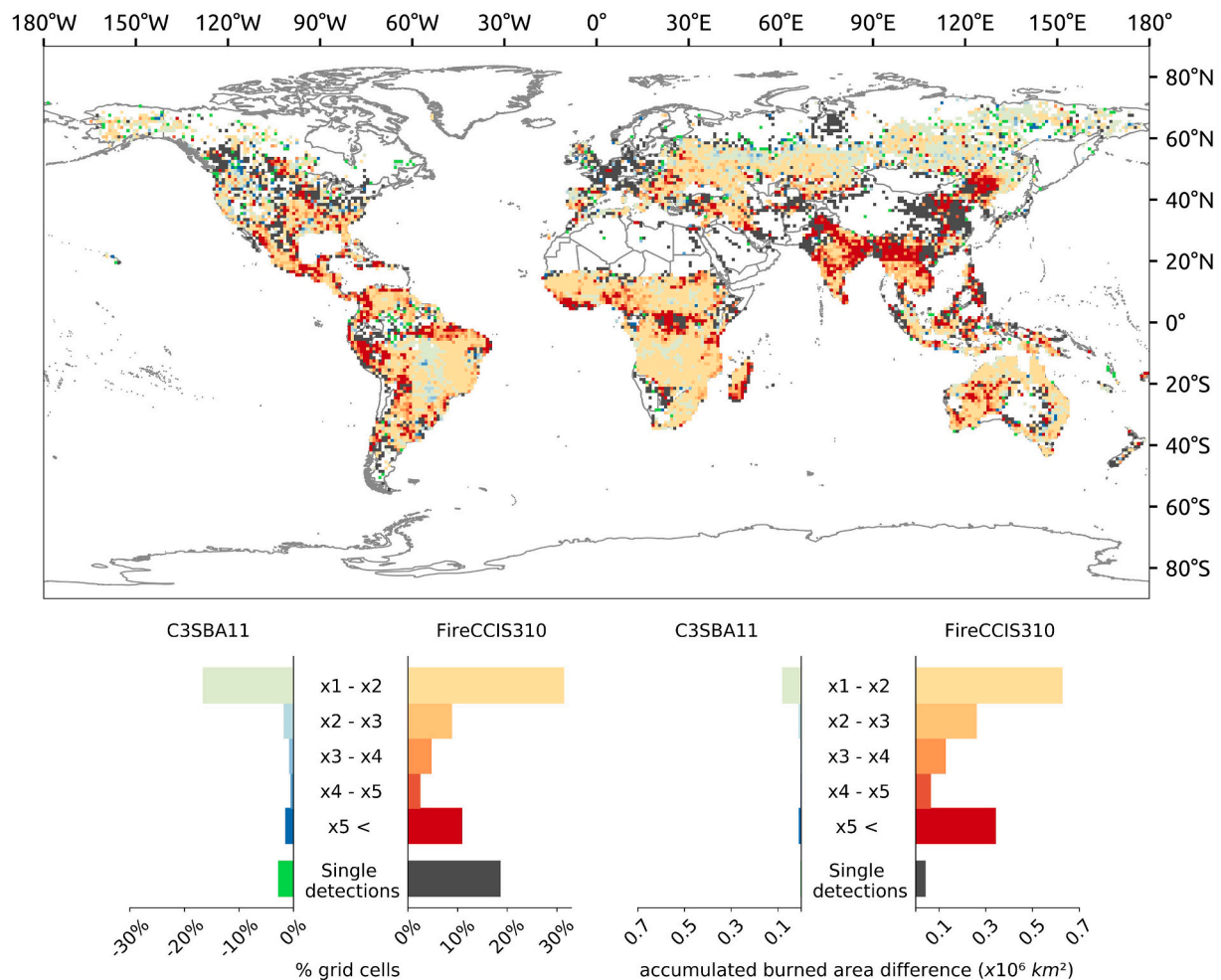
Fig. A3. Spatial distribution of the differences between the annual burned areas of the C3SBA11 and FireCCIS310 products at 1° spatial resolution. Each grid cell shows the quotient resulted from dividing the burned area of the product that detected the most by the one that detected the least. Thus, xN represents how many times more burned area was detected, being N the quotient. The red tones represent grid cells where FireCCIS310 detected more than C3SBA11, while the blue ones represent the contrary. The single detections are those cases where only one of the products detected burned area. (For interpretation of the references to colour in this figure legend, the reader is referred to the web version of this article.)

References

Abatzoglou, J.T., Williams, A.P., Boschetti, L., Zubkova, M., Kolden, C.A., 2018. Global patterns of interannual climate–fire relationships. Glob. Chang. Biol. 24, 5164–5175.

Alonso-Canas, I., Chuvieco, E., 2015. Global burned area mapping from ENVISAT-MERIS data. Remote Sens. Environ. 163, 140–152.

Amos, C., Petropoulos, G.P., Ferentinos, K.P., 2019. Determining the use of Sentinel-2A MSI for wildfire burning & severity detection. Int. J. Remote Sens. 40, 905–930.

Andela, N., Morton, D.C., Giglio, L., Chen, Y., van der Werf, G.R., Kasibhatla, P.S., DeFries, R.S., Collatz, G.J., Hantson, S., Kloster, S., Bachelet, D., Forrest, M., Lasslop, G., Li, F., Mangeon, S., Melton, J.R., Yue, C., Randerson, J.T., 2017. A human-driven decline in global burned area. Science 356, 1356.

Andela, N., Morton, D.C., Giglio, L., Paugam, R., Chen, Y., Hantson, S., van der Werf, G. R., Randerson, J.T., 2019. The Global Fire Atlas of individual fire size, duration, speed and direction. Earth Syst. Sci. Data 11, 529–552.

Astola, J., Kuosmanen, P., 1997. Fundamentals of Nonlinear Digital Filtering, (1st ed.). CRC Press.

Barbosa, P.M., Pereira, J.M.C., Grégoire, J.M., 1998. Compositing criteria for burned area assessment using multitemporal low resolution satellite data. Remote Sens. Environ. 65, 38–49.

Bastarrika, A., Chuvieco, E., Martín, M.P., 2011. Mapping burned areas from Landsat TM/ETM+ data with a two-phase algorithm: balancing omission and commission errors. Remote Sens. Environ. 115, 1003–1012.

Bin, W., Ming, L., Dan, J., Suju, L., Qiang, C., Chao, W., Yang, Z., Huan, Y., Jun, Z., 2019. A method of automatically extracting forest fire burned areas using Gf-1 remote sensing images. In: IGARSS 2019–2019 IEEE International Geoscience and Remote Sensing Symposium, pp. 9953–9955.

Boschetti, L., Roy, D.P., Giglio, L., Huang, H., Zubkova, M., Humber, M.L., 2019. Global validation of the collection 6 MODIS burned area product. Remote Sens. Environ. 235, 111490.

Boschetti, L., Roy, D.P., Justice, C.O., Giglio, L., 2010. Global assessment of the temporal reporting accuracy and precision of the MODIS burned area product. Int. J. Wildland Fire 19, 705–709.

Bowman, D., Williamson, G., Yebra, M., Lizundia-Loiola, J., Pettinari, M.L., Shah, S., Bradstock, R., Chuvieco, E., 2020. Wildfires: Australia needs national monitoring agency. Nature 584, 188–191.

Brassel, K.E., Reif, D., 1979. A procedure to generate Thiessen polygons. Geogr. Anal. 11, 289–303.

Bright, B.C., Hudak, A.T., Kennedy, R.E., Braaten, J.D., Henareh Khalyani, A., 2019. Examining post-fire vegetation recovery with Landsat time series analysis in three western North American forest types. Fire Ecol. 15, 8.

Campagnolo, M.L., Libonati, R., Rodrigues, J.A., Pereira, J.M.C., 2021. A comprehensive characterization of MODIS daily burned area mapping accuracy across fire sizes in tropical savannas. Remote Sens. Environ. 252, 112115.

Campagnolo, M.L., Oom, D., Padilla, M., Pereira, J.M.C., 2019. A patch-based algorithm for global and daily burned area mapping. Remote Sens. Environ. 232, 111288.

Chuvieco, E., Lizundia-Loiola, J., Pettinari, M.L., Ramo, R., Padilla, M., Tansey, K., Mouillot, F., Laurent, P., Storm, T., Heil, A., 2018. Generation and analysis of a new global burned area product based on MODIS 250 m reflectance bands and thermal anomalies. Earth Syst. Sci. Data 10, 2015–2031.

Chuvieco, E., Mouillot, F., van der Werf, G.R., San Miguel, J., Tanasse, M., Koutsias, N., García, M., Yebra, M., Padilla, M., Gitas, I., Heil, A., Hawbaker, T.J., Giglio, L., 2019. Historical background and current developments for mapping burned area from satellite Earth observation. Remote Sens. Environ. 225, 45–64.

Chuvieco, E., Ventura, G., Martín, M.P., Gomez, I., 2005. Assessment of multitemporal compositing techniques of MODIS and AVHRR images for burned land mapping. Remote Sens. Environ. 94, 450–462.

Csiszar, I., Schroeder, W., Giglio, L., Ellicott, E., Vadrevu, K.P., Justice, C.O., Wind, B., 2014. Active fires from the Suomi NPP Visible Infrared Imaging Radiometer Suite: Product status and first evaluation results. J. Geophys. Res. Atmos. 119, 803–816.

Defourny, P., Lamarche, C., Bontemps, S., De Maet, T., Van Bogaert, E., Moreau, I., Brockmann, C., Boettcher, M., Kirches, G., Wevers, J., Santoro, M., Ramoino, F., Arino, O., 2017. Land Cover Climate Change Initiative - Product User Guide v2. Issue 2.0. [online]. Available at: (last accesed on July 2022). http://maps.elie.ucl.ac.be/CCI/viewer/download/ESACCI-LC-Ph2-PUGv2_2.0.pdf.

Dice, L.R., 1945. Measures of the amount of ecologic association between species. Ecology 26, 297–302.

Dinerstein, E., Olson, D., Joshi, A., Vynne, C., Burgess, N.D., Wikramanayake, E., Hahn, N., Palminteri, S., Hedao, P., Noss, R., Hansen, M., Locke, H., Ellis, E.C., Jones, B., Barber, C.V., Hayes, R., Kormos, C., Martin, V., Crist, E., Sechrest, W., Price, L., Baillie, J.E.M., Weeden, D., Suckling, K., Davis, C., Sizer, N., Moore, R., Thau, D., Birch, T., Potapov, P., Turubanova, S., Tyukavina, A., de Souza, N., Pintea, L., Brito, J.C., Llewellyn, O.A., Miller, A.G., Patzelt, A., Ghazanfar, S.A., Timberlake, J., Klöser, H., Shennan-Farpón, Y., Kindt, R., Lillesø, J.-P.B., van Breugel, P., Graudal, L., Voge, M., Al-Shammari, K.F., Saleem, M., 2017. An ecoregion-based approach to protecting half the terrestrial realm. Bioscience 67, 534–545.

Fanin, T., van der Werf, G.R., 2015. Relationships between burned area, forest cover loss, and land cover change in the Brazilian Amazon based on satellite data. Biogeosciences 12, 6033–6043.

Fernández-Manso, A., Quintano, C., 2020. A synergetic approach to burned area mapping using maximum entropy modeling trained with hyperspectral data and VIIRS hotspots. Remote Sens. 12.

Franquesa, M., Lizundia-Loiola, J., Stehman, S.V., Chuvieco, E., 2022. Using long temporal reference units to assess the spatial accuracy of global satellite-derived burned area products. Remote Sens. Environ. 269, 112823.

Franquesa, M., Vanderhoof, M.K., Stavrakoudis, D., Gitas, I., Roteta, E., Padilla, M., Chuvieco, E., 2020. BARD: a global and regional validation burned area database, V5 e-cienciaDatos.

Franquesa, M., Vanderhoof, M.K., Stavrakoudis, D., Gitas, I.Z., Roteta, E., Padilla, M., Chuvieco, E., 2020b. Development of a standard database of reference sites for validating global burned area products. Earth Syst. Sci. Data 12, 3229–3246.

Giglio, L., Boschetti, L., Roy, D.P., Humber, M.L., Justice, C.O., 2018. The collection 6 MODIS burned area mapping algorithm and product. Remote Sens. Environ. 217, 72–85.

Giglio, L., Loboda, T., Roy, D.P., Quayle, B., Justice, C.O., 2009. An active-fire based burned area mapping algorithm for the MODIS sensor. Remote Sens. Environ. 113, 408–420.

Giglio, L., Schroeder, W., Justice, C.O., 2016. The collection 6 MODIS active fire detection algorithm and fire products. Remote Sens. Environ. 178, 31–41.

Hawbaker, T.J., Vanderhoof, M.K., Schmidt, G.L., Beal, Y.-J., Picotte, J.J., Takacs, J.D., Falgout, J.T., Dwyer, J.L., 2020. The Landsat Burned Area algorithm and products for the conterminous United States. Remote Sens. Environ. 244, 111801.

Henocq, C., North, P., Heckel, A., Ferron, S., Lamquin, N., Dransfeld, S., Bourg, L., Ramon, J., 2018. OLCI/SLSTR SYN L2 algorithm and products overview. In: IGARSS 2018 - 2018 IEEE International Geoscience and Remote Sensing Symposium, pp. 8723–8726.

Jacques, D.C., Kergoat, L., Hiernaux, P., Mougin, E., Defourny, P., 2014. Monitoring dry vegetation masses in semi-arid areas with MODIS SWIR bands. Remote Sens. Environ. 153, 40–49.

Justice, C.O., Román, M.O., Csiszar, I., Vermote, E.F., Wolfe, R.E., Hook, S.J., Friedl, M., Wang, Z., Schaaf, C.B., Miura, T., Tschudi, M., Riggs, G., Hall, D.K., Lyapustin, A.I., Devadiga, S., Davidson, C., Masuoka, E.J., 2013. Land and cryosphere products from Suomi NPP VIIRS: Overview and status. J. Geophys. Res. Atmos. 118, 9753–9765.

Kelly, L.T., Brotons, L., 2017. Using fire to promote biodiversity. Science 355, 1264.

Laurent, P., Mouillot, F., Yue, C., Ciais, P., Moreno, M.V., Nogueira, J.M., 2018. FRY, a global database of fire patch functional traits derived from space-borne burned area products. Sci. Data 5, 180132.

Liu, J., Maeda, E.E., Wang, D., Heiskanen, J., 2021. Sensitivity of Spectral Indices on Burned Area Detection using Landsat Time Series in Savannas of Southern Burkina Faso. Remote Sens. 13.

Liu, T., Crowley, M.A., 2021. Detection and impacts of tiling artifacts in MODIS burned area classification. IOP SciNotes 2, 014003.

Lizundia-Loiola, J., Franquesa, M., Boettcher, M., Kirches, G., Pettinari, M.L., Chuvieco, E., 2021. Implementation of the Burned Area Component of the Copernicus Climate Change Service: From MODIS to OLCI Data. Remote Sens. 13.

Lizundia-Loiola, J., Otón, G., Ramo, R., Chuvieco, E., 2020. A spatio-temporal active-fire clustering approach for global burned area mapping at 250 m from MODIS data. Remote Sens. Environ. 236, 111493.

Long, T., Zhang, Z., He, G., Jiao, W., Tang, C., Wu, B., Zhang, X., Wang, G., Yin, R., 2019. 30 m Resolution global annual burned area mapping based on landsat images and google earth engine. Remote Sens. 11.

Melchiorre, A., Boschetti, L., 2018. Global analysis of burned area persistence time with MODIS data. Remote Sens. 10.

Merchant, C.J., Paul, F., Popp, T., Ablain, M., Bontemps, S., Defourny, P., Hollmann, R., Lavergne, T., Laeng, A., de Leeuw, G., 2017. Uncertainty information in climate data records from Earth observation. Earth Syst.Sci. Data 9.

Miettinen, J., 2007. Variability of fire-induced changes in MODIS surface reflectance by land-cover type in Borneo. Int. J. Remote Sens. 28, 4967–4984.

Oliva, P., Schroeder, W., 2015. Assessment of VIIRS 375m active fire detection product for direct burned area mapping. Remote Sens. Environ. 160, 144–155.

Otón, G., Lizundia-Loiola, J., Pettinari, M.L., Chuvieco, E., 2021. Development of a consistent global long-term burned area product (1982–2018) based on AVHRR-LTDR data. Int. J. Appl. Earth Obs. Geoinf. 103, 102473.

Otsu, N., 1979. A threshold selection method from gray-level histograms. IEEE Trans. Syst. Man Cybernet. 9, 62–66.

Padilla, M., Olofsson, P., Stehman, S.V., Tansey, K., Chuvieco, E., 2017. Stratification and sample allocation for reference burned area data. Remote Sens. Environ. 203, 240–255.

Ramo, R., Roteta, E., Bistinas, I., van Wees, D., Bastarrika, A., Chuvieco, E., van der Werf, G.R., 2021. African burned area and fire carbon emissions are strongly impacted by small fires undetected by coarse resolution satellite data. Proc. Natl. Acad. Sci. 118, e2011160118.

Randerson, J., Chen, Y., Werf, G., Rogers, B., Morton, D., 2012. Global burned area and biomass burning emissions from small fires. J. Geophys. Res. Biogeosci. 117 - G04012, 1–23.

Reid, C.E., Brauer, M., Johnston, F.H., Jerrett, M., Balmes, J.R., Elliott, C.T., 2016. Critical review of health impacts of wildfire smoke exposure. Environ. Health Perspect. 124, 1334–1343.

Roteta, E., Bastarrika, A., Ibisate, A., Chuvieco, E., 2021. A preliminary global automatic burned-area algorithm at medium resolution in google earth engine. Remote Sens. 13.

Roteta, E., Bastarrika, A., Padilla, M., Storm, T., Chuvieco, E., 2019. Development of a Sentinel-2 burned area algorithm: generation of a small fire database for sub-Saharan Africa. Remote Sens. Environ. 222, 1–17.

Roy, D.P., Huang, H., Boschetti, L., Giglio, L., Yan, L., Zhang, H.H., Li, Z., 2019. Landsat-8 and Sentinel-2 burned area mapping - a combined sensor multi-temporal change detection approach. Remote Sens. Environ. 231, 111254.

Santos, F.L.M., Libonati, R., Peres, L.F., Pereira, A.A., Narciso, L.C., Rodrigues, J.A., Oom, D., Pereira, J.M.C., Schroeder, W., Setzer, A.W., 2020. Assessing VIIRS capabilities to improve burned area mapping over the Brazilian Cerrado. Int. J. Remote Sens. 41, 8300–8327.

Schroeder, W., Giglio, L., 2018. Visible Infrared Imaging Radiometer Suite (VIIRS) 375 m & 750 m active fire products. In: Product User's Guide Version 1.4. NASA VIIRS Land Science Investigator Processing System (SIPS).

Schroeder, W., Oliva, P., Giglio, L., Csiszar, I.A., 2014. The New VIIRS 375 m Active Fire Detection Data Product: Algorithm Description and Initial Assessment. Remote Sens. Environ. 143, 85–96.

Sousa, A.M.O., Pereira, J.M.C., Silva, J.M.N., 2003. Evaluating the performance of multitemporal image compositing algorithms for burned area analysis. Int. J. Remote Sens. 24, 1219–1236.

Trigg, S., Flasse, S., 2001. An evaluation of different bi-spectral spaces for discriminating burned shrub-savannah. Int. J. Remote Sens. 22, 2641–2647.

Urbanski, S., Nordgren, B., Albury, C., Schwert, B., Peterson, D., Quayle, B., Hao, W.M., 2018. A VIIRS direct broadcast algorithm for rapid response mapping of wildfire burned area in the western United States. Remote Sens. Environ. 219, 271–283.

van der Werf, G.R., Randerson, J.T., Giglio, L., Van Leeuwen, T.T., Chen, Y., Rogers, B. M., Mu, M., Van Marle, M.J.E., Morton, D.C., Collatz, G.J., 2017. Global fire emissions estimates during 1997–2016. Earth Syst. Sci. Data 9, 697–720.

Waigl, C.F., Stuefer, M., Prakash, A., Ichoku, C., 2017. Detecting high and low-intensity fires in Alaska using VIIRS I-band data: An improved operational approach for high latitudes. Remote Sens. Environ. 199, 389–400.

Xu, W., Wooster, M.J., Polehampton, E., Yemelyanova, R., Zhang, T., 2021. Sentinel-3 active fire detection and FRP product performance - Impact of scan angle and SLSTR middle infrared channel selection. Remote Sens. Environ. 261, 112460.

Zhang, Q.F., Pavlic, G., Chen, W.J., Fraser, R., Leblanc, S., Cihlar, J., 2005. A semi-automatic segmentation procedure for feature extraction in remotely sensed imagery. Comput. Geosci. 31, 289–296.